Estimating the turbulent kinetic energy dissipation rate from one-dimensional velocity measurements in time

Marcel Schröder[1,2], Tobias Bätge[1,2], Eberhard Bodenschatz[1,2,3], Michael Wilczek[1,4], and Gholamhossein Bagheri[1]

[1]Max Planck Institute for Dynamics and Self-Organization (MPIDS), Am Faßberg 17, 37077 Göttingen, Germany
[2]Faculty of Physics, Georg August University Göttingen, Friedrich-Hund-Platz 1, 37077 Göttingen, Germany
[3]Physics Department, Cornell University, 523 Clark Hall, Ithaca, NY, USA
[4]Theoretical Physics I, University of Bayreuth, Universitätsstr. 30, 95447 Bayreuth, Germany

Correspondence: Gholamhossein Bagheri (gholamhossein.bagheri@ds.mpg.de)

Abstract. The turbulent kinetic energy dissipation rate is one of the most important quantities characterizing turbulence. Experimental studies of a turbulent flow in terms of the energy dissipation rate often rely on one-dimensional measurements of the flow velocity fluctuations in time. In this work, we first use direct numerical simulation of stationary homogeneous isotropic turbulence at Taylor-scale Reynolds numbers $74 \leq R_\lambda \leq 321$ to evaluate different methods for inferring the energy dissipation rate from one-dimensional velocity time records. We systematically investigate the influence of the finite turbulence intensity and the misalignment between the mean flow direction and the measurement probe, and derive analytical expressions for the errors associated with these parameters. We further investigate how statistical averaging for different time windows affects the results as a function of R_λ. The results are then combined with Max Planck Variable Density Turbulence Tunnel hot-wire measurements at $147 \leq R_\lambda \leq 5864$ to investigate flow conditions similar to those in the atmospheric boundary layer. Finally, practical guidelines for estimating the energy dissipation rate from one-dimensional atmospheric velocity records are given.

1 Introduction

Turbulence is fundamental to many natural and engineering processes, such as transport of heat and moisture in the Earth's atmosphere (e.g. Wyngaard, 1992; Garratt, 1994; Muschinski and Lenschow, 2001; Fairall and Larsen, 1986; Hsieh and Katul, 1997), wind energy conversion (Smalikho et al., 2013), entrainment and mixing (e.g. Warhaft, 2000; Sreenivasan, 2004; Deshpande et al., 2009; Gerber et al., 2008, 2013; Siebert et al., 2013; Fodor and Mellado, 2020), and warm rain initiation (e.g. Shaw, 2003; Devenish et al., 2012; Pumir and Wilkinson, 2016; Li et al., 2020), to name just a few. In three-dimensional turbulence, the kinetic energy is typically injected into the flow at the largest scales and successively transferred to smaller eddies by means of the direct energy cascade. At the smallest scales characterized by the Kolmogorov length scale (or the dissipation scale) η_K, kinetic energy is dissipated by viscous effects at the energy dissipation rate (a list of all the parameters and symbols used in this study can be found in Tables A1 and A2). The energy dissipation rate is one of the most fundamental quantities in turbulence and is used to estimate many relevant features of a turbulent flow, such as the Kolmogorov length scale η_K, the Taylor microscale λ, the Taylor-scale Reynolds number R_λ and, by means of dimensional estimates, the energy injection scale.

The instantaneous energy dissipation field $\epsilon_0(\boldsymbol{x}, t)$, which is a function of the fluid kinematic viscosity ν and the velocity gradient tensor, is highly intermittent with strong small-scale fluctuations (Pope, 2000; Davidson, 2015, and references therein),
which are at the core of the intermittency problem in turbulence (Sreenivasan and Antonia, 1997; Muschinski et al., 2004; Buaria et al., 2019). By "instantaneous" we here want to emphasize that ϵ_0 is the energy dissipation rate at one point in space and time within the flow. It also plays an important role in turbulent mixing in reacting flows (e.g., Sreenivasan, 2004; Hamlington et al., 2012; Sreenivasan, 2019) or turbulence-induced rain initiation in warm clouds (Devenish et al., 2012). $\epsilon_0(\boldsymbol{x}, t)$, however, is extremely difficult to measure experimentally because it requires complete knowledge of the three-dimensional velocity field with spatial/temporal resolution that can resolve scales smaller than or at least comparable to Kolmogorov scales.

Apart from the instantaneous dissipation field $\epsilon_0(\boldsymbol{x}, t)$, the energy dissipation in a turbulent flow can be statistically described by either the local or global mean energy dissipation rate, which are both important. Local volume averages of the instantaneous dissipation field $\langle\epsilon_0\rangle_R$ and related surrogates, e.g., longitudinal, transverse or off-diagonal components of the velocity gradient, can capture intermittency of turbulence (Lefeuvre et al., 2014; Almalkie and de Bruyn Kops, 2012, and references therein). The local volume averages of the dissipation field converge to the global mean energy dissipation rate $\langle\epsilon\rangle$ for statistically converged sampling. $\langle\epsilon\rangle$ can be used to parameterize the statistics of statistically homogeneous and locally isotropic turbulence based on the Kolmogorov's phenomenology (K41) (Kolmogorov, 1941). Note that even if the global mean energy dissipation rate $\langle\epsilon\rangle$ is known, it is also of high interest to know how locally averaged dissipation rates $\langle\epsilon_0\rangle_R$ differ from the global mean energy dissipation rate $\langle\epsilon\rangle$. For example, the local dissipation rate determines whether droplets in a cloud behave as tracer or inertial particles, which in turn can affect the probability of collision/coalescence of the droplets and thus the likelihood of precipitation initiation (e.g., see Shaw, 2003).

For a statistically stationary homogeneous isotropic (SHI) turbulent flow, $\langle\epsilon\rangle$ can be estimated from time-dependent single-point one-dimensional velocity measurements through different methods, such as longitudinal or transverse velocity gradients (Wyngaard and Clifford, 1977; Elsner and Elsner, 1996; Antonia, 2003; Siebert et al., 2006, among others), inertial-range scaling laws comprising the famous 4/5 law (Kolmogorov, 1941, 1991; Muschinski et al., 2001), counting zero-crossings of the velocity fluctuation time series (Sreenivasan et al., 1983; Wacławczyk et al., 2017) or dimensional arguments (e.g. Taylor, 1935; McComb et al., 2010; Vassilicos, 2015). These methods usually invoke Taylor's hypothesis to map temporal signals onto spatial signals, which requires a *sufficiently small* turbulence intensity. The turbulence intensity is defined as the ratio of the root mean square velocity fluctuations $\sigma_{u'}$ to the mean velocity U. When all of these criteria are met, single-point velocity measurements with hot-wire anemometers at a high temporal resolution have been shown to be suitable for accurately estimating the global energy dissipation rate (see also below) (Lewis et al., 2021; Sinhuber, 2015; Elsner and Elsner, 1996; Antonia, 2003; Frehlich et al., 2003). However, in atmospheric flows, the assumption of *ideal* stationary homogeneous isotropic turbulence needs to be very carefully considered, as for example thermals, change in local weather conditions and of course the diurnal cycle may lead to non-stationarity and inhomogeneity.

Then the global mean energy dissipation rate $\langle\epsilon\rangle$ is not representative as the turbulence can be highly time- and space-dependent even at the energy injection scales. As a result, one needs to calculate a local $\langle\epsilon_0\rangle_\tau$ and $\langle\epsilon_0\rangle_R$, respectively, based on velocity statistics for a *properly chosen* averaging window τ in time or R in space, which is short enough for resolving the tem-

poral or spatial variations but also long enough to obtain statistically representative values with *acceptable* systematic and/or random errors (e.g. Wyngaard, 1992; Lenschow et al., 1994). Therefore, a conflict arises with respect to the averaging time between resolving small-scale features of a turbulent flow and statistical convergence under non-stationary and inhomogeneous conditions.

In the case of atmospheric flows, in *situ* measurements made via airborne (Malinowski et al., 2013; Siebert et al., 2006, 2013; Muschinski et al., 2004; Frehlich et al., 2004; Nowak et al., 2021; Dodson and Small Griswold, 2021, e.g.) as well as ground-based (Chamecki and Dias, 2004; O'Connor et al., 2010; Risius et al., 2015; Siebert et al., 2015, e.g.) platforms typically can only resolve the coarse-grained time series of the local mean energy dissipation rate $\langle \epsilon_0 \rangle_\tau$. However, it remains unclear how large the errors in estimating the coarse-grained time series of the local mean energy dissipation rate are due to individual choices of the averaging window, since there is currently no high-resolution three-dimensional velocity measurement available during in *situ* measurements to serve as the ground truth,. In the absence of a ground-truth reference, the comparison between different methods was used as the next best benchmark for validity of a given method (Siebert et al., 2010; Wacławczyk et al., 2020; Siebert et al., 2006; Risius et al., 2015; Wacławczyk et al., 2017), which in some cases makes the interpretation of the data difficult due to the large discrepancies between the estimates obtained by different methods. As an example, Wacławczyk et al. (2020) found deviations of about 5%-50% for estimating the mean energy dissipation rate depending on the method and averaging windows using synthetic data modeled via a von Karman spectrum. Another example is the work of Akinlabi et al. (2019), who found that estimates of mean energy dissipation rate by one-dimensional longitudinal velocity can differ by a factor of 2 to 3 from those calculated using direct numerical simulations (DNS), depending on the method used.

Our literature review indicates that a systematic investigation is still needed to fully understand how the choice of averaging window, analysis methods, turbulence intensity and large-scale random flow velocities can influence estimating the mean energy dissipation rate and its deviations from the instantaneous energy dissipation rate. To this end, we systematically benchmark different techniques available in the literature using fully resolved DNS of statistically stationary, homogeneous, isotropic turbulence. Since the full dissipation field is available from DNS, this approach provides ground-truth reference for comparisons to the various estimation techniques. To bridge the gap between typical R_λ of DNS and atmospheric flows, we use high-resolution measurements of the longitudinal velocity components of the Variable Density Turbulence Tunnel (VDTT) (Bodenschatz et al., 2014; Sinhuber, 2015; Küchler et al., 2019) at various Taylor Reynolds number R_λ between 140 and 6000. The impact of turbulence intensity, large-scale random sweeping velocities, size of averaging window, Reynolds number and also possible experimental imperfections, such as anemometer misalignment are investigated in detail. Our work aims to be a step towards the goal of extracting the time-dependent energy dissipation rate from non-ideal naturally-occurring turbulent flows mitigating the impact of non-ideal features of the flow, e.g., anisotropy or inhomogeneity. In Sect. 2, we first define the central statistical quantities and the individual methods for estimating the energy dissipation rate in detail. An analysis of the individual methods including discrepancies, errors due to finite turbulence intensity, and alignment errors are discussed in Sect. 3 followed by a summary of our findings.

2 Methods

Let $\boldsymbol{u}(\boldsymbol{x},t) = u_1(\boldsymbol{x},t)\boldsymbol{e}_1 + u_2(\boldsymbol{x},t)\boldsymbol{e}_2 + u_3(\boldsymbol{x},t)\boldsymbol{e}_3$ denote the three-dimensional velocity vector of the turbulent flow, where $\boldsymbol{x} = x_1\boldsymbol{e}_1 + x_2\boldsymbol{e}_2 + x_3\boldsymbol{e}_3$ are the components of the Cartesian coordinate system and t is the time. We assume that the streamwise direction of the global-mean flow $\boldsymbol{U}$ is in the direction of $\boldsymbol{e}_1$ such that $\boldsymbol{U} = U\boldsymbol{e}_1$ is (by definition) constant in space and time.
We refer to $\boldsymbol{e}_1$ as the *longitudinal* direction and the components normal to that, i.e., $\boldsymbol{e}_2$ and $\boldsymbol{e}_3$, as the *transverse* directions of the flow. As mentioned earlier, many experimental setups record only a one-dimensional flow velocity at one location and as a function of time. We consider this one-dimensional velocity time record to be in the longitudinal flow direction unless otherwise stated, e.g., when the probe misalignment is investigated. In the following, we first introduce different averaging principles that can be used to analyze turbulence statistics and Taylor's frozen hypothesis, and then present the commonly used methods for extracting the energy dissipation rate. An introduction of the basic statistical description of turbulent flows is provided in the appendix (Sec. A) for the sake of completeness.

2.1 On Averaging, Reynolds Decomposition and Taylor's Hypothesis

Most methods used to retrieve the dissipation rate require spatially resolved velocity statistics although the velocity is recorded only at a single point and as a function of time in many experiments. Therefore, prior to estimating the energy dissipation rate, the one-dimensional velocity time-record should be first mapped onto a spatially resolved velocity field. This is achieved by invoking Taylor's hypothesis (Taylor, 1938), which requires a Reynolds decomposition of the velocity time-record by separating the velocity fluctuations from the mean velocity. To perform the Reynolds decomposition, we first have to clarify what is meant by the mean velocity.

Generally, we have to distinguish between the global mean velocity $\boldsymbol{U} = \langle\boldsymbol{u}(\boldsymbol{x},t)\rangle = U\boldsymbol{e}_1$, the volume-averaged velocity $\langle\boldsymbol{u}(\boldsymbol{x},t)\rangle_R$ over a sphere of radius R, the time-averaged velocity $\langle\boldsymbol{u}(\boldsymbol{x},t)\rangle_\tau$ over a time interval τ, and the ensemble-averaged velocity $\langle\boldsymbol{u}(\boldsymbol{x},t)\rangle_N$ over N realizations (Wyngaard, 2010; Pope, 2000, among others). In this work, $\langle\cdot\rangle$ denotes the global mean, i.e., for infinitely large averaging windows in time or space. Thus, $\boldsymbol{U}$ is by definition independent of time and space, which in reality is valid only when $\boldsymbol{u}(\boldsymbol{x},t)$ is statistically stationary and homogeneous. Implicitly, $\langle\boldsymbol{u}(\boldsymbol{x},t)\rangle_R = 3/(4\pi R^3)\iiint_0^R \mathrm{d}\boldsymbol{x}\,\boldsymbol{u}(\boldsymbol{x},t)$ and $\langle\boldsymbol{u}(\boldsymbol{x},t)\rangle_\tau = \frac{1}{\tau}\int_{-\tau/2}^{\tau/2}\mathrm{d}t'\boldsymbol{u}(\boldsymbol{x},t')$ are, respectively, local volume and time averages as both R and τ are typically finite. In the limit of $R,\tau \to \infty$, $\langle\boldsymbol{u}(\boldsymbol{x},t)\rangle_R$ and $\langle\boldsymbol{u}(\boldsymbol{x},t)\rangle_\tau$ tend to $\boldsymbol{U}$. For repeatable experiments where identical experimental conditions are guaranteed, $\langle\boldsymbol{u}(\boldsymbol{x},t)\rangle_N$ tends to $\boldsymbol{U}$ when $N \to \infty$.

The mean of a one-dimensional velocity time-record in the longitudinal direction U_τ here is defined by

$$U_\tau = \langle u_1(t)\rangle_\tau = \frac{1}{\tau}\int\limits_{-\tau/2}^{\tau/2}\mathrm{d}t'u_1(t')\,, \tag{1}$$

such that the global mean $U = \lim_{\tau\to\infty}U_\tau$, where τ is the *averaging window*. It should be noted that the global mean of the transverse velocity will be equal to zero, i.e., $\langle u_{2,3}(t)\rangle_\tau = 0$ when $\tau \to \infty$, since here it is assumed that they are orthogonal

to the mean flow direction. According to the Reynolds decomposition, the longitudinal velocity time record is composed of the mean velocity U and the random velocity fluctuation component $u_1'(t) = u_1(t) - U$ so that the mean of the longitudinal velocity fluctuations $\langle u_1'(t) \rangle = 0$.

In certain circumstances, it is possible to map $u_1'(t)$ from time to space coordinates by applying the Taylor's (frozen-eddy) hypothesis (Taylor, 1938; Wyngaard, 2010), which relates temporal and spatial velocity statistics. Taylor argues that eddies can be regarded as *frozen* in time if they are passing the probing volume much faster than they evolve in time. This is the case if the turbulence intensity $I = \sigma_{u_1'}/U$ is much smaller than the unity, i.e., $I \ll 1$, where $\sigma_{u_1'} = \langle u_1'^2 \rangle^{1/2}$ is the Root-Mean-Square (RMS) velocity fluctuation. Then, the series of time lags $\Delta t = t - t_0$ relative to the start time t_0 is mapped onto a distance vector with $\boldsymbol{x} = \boldsymbol{x}_0 + U\Delta t \, \boldsymbol{e}_1$ (Taylor, 1938), where $\boldsymbol{x}_0$ is the initial position at time t_0. This approach is found to be reliable for $I \lesssim 0.25$ (Nobach and Tropea, 2012; Wilczek et al., 2014; Risius et al., 2015) while it has been shown to fail when $I > 0.5$ (Willis and Deardorff, 1976). The application of Taylor's hypothesis is inaccurate in case of large-scale variations of the velocity fluctuation field comparable to the mean velocity, which are known as "random sweeping velocity" (Kraichnan, 1964; Tennekes, 1975). Complicating the estimation of the mean velocity, random sweeping causes the mean energy dissipation rate to be consistently overestimated (Lumley, 1965; Wyngaard and Clifford, 1977).

One way to cope with non-stationary velocity time records is to evaluate the mean velocity for a subset of this signal. If the averaging time τ is finite, the time average U_τ may differ from the mean velocity U causing a systematic bias in the subsequent data analysis. The estimation variance of the time average U_τ can be analytically expressed as (Wyngaard, 2010; Pope, 2000, among others)

$$\langle (U_\tau - U)^2 \rangle \approx \frac{2 \langle u_1'^2 \rangle T}{\tau} , \tag{2}$$

where T is the integral time scale and $\langle u_1'^2 \rangle$ the variance of the velocity time series. Notably, the size of the averaging window has to be large enough such that it fulfills $\langle u_1'(t) \rangle_\tau \approx 0$ to apply the Reynolds decomposition.

2.2 Estimating the Energy Dissipation Rate

The energy dissipation rate can be derived from various statistical quantities. A non-exhaustive list of the most common methods applicable to single-point measurements is shown in Table 1. Details of selected methods considered in this study are presented in the following subsections. If not explicitly mentioned, the averages denoted with $\langle \cdot \rangle$ are defined globally.

range	Dissipation estimate (Eq.)	symbol	definition	assumption
dissipative sub-range	instantaneous (3)	ϵ_0	$2\nu\left(s_{ij}s_{ij}\right)$	
	(local) volume average (4)	$\epsilon_R(\boldsymbol{x},t)$	$\frac{3}{4\pi R^3}\iiint_{\mathcal{V}(R)}\epsilon_0(\boldsymbol{x}+\boldsymbol{r},t)\mathrm{d}\boldsymbol{r}$	SHI
	(longitudinal) gradient (6)	ϵ_G	$15\nu\left\langle\left(\frac{\partial u_1'(\boldsymbol{x})}{\partial x_1}\right)^2\right\rangle$	SHI
	2nd-order SF (dissipation range) *	ϵ_{D2}	$15\nu D_{LL}(r)/r^2$	SHI, $r\lesssim\eta_K$
	zero-crossings *	ϵ_+	$15\pi^2\nu\langle u_1'^2\rangle N_L^2$	SHI
inertial sub-range	4/5 law * ((7), $n=3$)	ϵ_{I3}	$-5/4 D_{LLL}(r)/r$	SHI, K41
	2nd-order SF (inertial range) ((7), $n=2$)	ϵ_{I2}	$\left(D_{LL}(r)/C_2\right)^{3/2}/r$	SHI, K41
	spectral (9)	ϵ_S	$\left(\frac{\kappa_1^{5/3}E_{11}(\kappa_1)}{18/55 C_K}\right)^{3/2}$	SHI, K41
	cutoff filter *	ϵ_C	$\left(\frac{2}{3}\frac{2\langle u_C'^2\rangle}{18/55 C_K\left(\kappa_{1,\mathrm{low}}^{-2/3}-\kappa_{1,\mathrm{up}}^{-2/3}\right)}\right)^{3/2}$	SHI, K41
energy injection scale	scaling argument (10)	ϵ_L	$C_\epsilon\sigma_{u_1'}^3/L_{11}$	SHI
	global mean (5)	$\langle\epsilon\rangle$	$\lim_{R\to\infty}\langle\epsilon_0(\boldsymbol{x},t)\rangle_R$	SHI

Table 1. Various definitions of the energy dissipation rate from the dissipative and inertial sub-range to the energy injection range. Here, the definitions for various dissipation estimates are given in the space or wavenumber domain where ν is the viscosity, s_{ij} is the velocity fluctuation strain rate tensor, R is the radius of the averaging volume $\mathcal{V}(R)$ (window size for 1D data), $u_1'(\boldsymbol{x})$ is the longitudinal velocity fluctuation field along $\boldsymbol{e}_1$, $D_{L...L}(r)$ is the nth-order longitudinal Structure Function (SF) for distance r, $\langle u_1'^2\rangle$ is the variance of $u_1'(\boldsymbol{x})$, $\sigma_{u_1'}$ is the standard deviation of $u_1'(\boldsymbol{x})$, N_L is the number of zero crossings of a velocity fluctuation signal per unit length, $C_2\approx 2$, $E_{11}(\kappa_1)$ is the one-dimensional energy spectrum with wavenumber κ_1, $C_K\approx 1.5$, $\langle u_C'^2\rangle$ is the variance of a band-pass filtered signal for wavenumbers $\kappa_1\in[\kappa_{1,\mathrm{low}},\kappa_{1,\mathrm{up}}]$, C_ϵ is the dissipation constant, L_{11} is the longitudinal integral scale, and η_K is the Kolmogorov length scale. Dissipation estimates indicated with * are not considered in detail in this work. The assumptions of stationarity (S), homogeneity (H), local isotropy (I) and Kolmogorov's second similarity hypothesis from 1941 (K41) are represented by their individual abbreviations. References are given in the corresponding sections in the main text.

2.2.1 Dissipative sub-range

Proceeding from the Navier-Stokes equations for an incompressible, Newtonian fluid, the instantaneous energy dissipation rate is given by $2\nu\left(S_{ij}S_{ij}\right)$ (e.g., Pope, 2000; Davidson, 2015). As the velocity gradients are dominated by small-scale fluctuations, turbulent kinetic energy is dissipated into heat at small scales. Therefore, the contribution of large-scale variations of the velocity is small compared to the contribution of the small scales (Pope, 2000; Elsner and Elsner, 1996). Hence, the instantaneous energy dissipation rate can be defined in terms of the velocity fluctuations only, i.e., replacing S_{ij} by the fluctuation strain rate tensor $s_{ij}=(\partial u_i'(\boldsymbol{x},t)/\partial x_j+\partial u_j'(\boldsymbol{x},t)/\partial x_i)/2$ (Pope, 2000):

$$\epsilon_0(\boldsymbol{x},t)=2\nu\left(s_{ij}s_{ij}\right).\tag{3}$$

6

Averaged over a sphere with radius R and volume $\mathcal{V}(R)$, the (local) volume average of the instantaneous energy dissipation rate is (Pope, 2000)

$$\epsilon_R(\boldsymbol{x},t) = \langle \epsilon_0(\boldsymbol{x},t) \rangle_R = \frac{3}{4\pi R^3} \iiint\limits_{\mathcal{V}(R)} \epsilon_0(\boldsymbol{x}+\boldsymbol{r},t) \mathrm{d}\boldsymbol{r} \, . \tag{4}$$

The local volume average $\epsilon_R(\boldsymbol{x},t)$ converges to the global mean energy dissipation rate if R tends to infinity (Pope, 2000):

$$\langle \epsilon \rangle = \lim_{R \to \infty} \langle \epsilon_0(\boldsymbol{x},t) \rangle_R = -\nu \lim_{|\boldsymbol{r}| \to 0} \partial_{r_j}^2 R_{ii}(\boldsymbol{r},t) \, , \tag{5}$$

where the right-hand-side follows from partial integration and R_{ii} is the diagonal component of the velocity covariance tensor, see Eq. (A1) and Table A1. In experiments, it is often not possible to measure $\epsilon_0(\boldsymbol{x},t)$. Under the assumption of statistically homogeneous and isotropic turbulence, the volume/time-averaged energy dissipation rate are typically inferred from one-dimensional surrogates (Taylor, 1935; Elsner and Elsner, 1996; Siebert et al., 2006; Almalkie and de Bruyn Kops, 2012; Champagne, 1978; Donzis et al., 2008, among others), such as from the longitudinal velocity gradient (hence, the subscript G):

$$\epsilon_G = -15\nu \lim_{|\boldsymbol{r}| \to 0} \partial_{r_1}^2 R_{11}(\boldsymbol{r},t) = 15\nu \left\langle \left(\frac{\partial u_1'(\boldsymbol{x},t)}{\partial x_1} \right)^2 \right\rangle = \frac{15\nu}{U^2} \left\langle \left(\frac{\partial u_1'(t)}{\partial t} \right)^2 \right\rangle , \tag{6}$$

where the mapping between space and time domains is possible by applying Taylor's hypothesis if $\sigma_{u_1'}/U \ll 1$ and R_{11} is the longitudinal component of the velocity covariance tensor defined in Eq. (A1) (Siebert et al., 2006; Muschinski et al., 2004). The relationship shown in Eq. (6) is often called the "direct" method in the literature (Muschinski et al., 2004; Siebert et al., 2006, e.g.) and requires a spatial resolution higher than the Kolmogorov length scale η_K to be accurate to $\sim 10\%$ (cf. Fig. A8). The deviation of ϵ_G from its global mean $\langle \epsilon \rangle$ depends quadratically on the turbulence intensity (Lumley, 1965; Wyngaard and Clifford, 1977; Champagne, 1978; Muschinski et al., 2004).

2.2.2 Inertial sub-range: structure functions

Kolmogorov's second similarity hypothesis from 1941 (Kolmogorov, 1941) provides another method for estimating the energy dissipation rate in the inertial range. Based on the inertial range scaling of the nth-order longitudinal structure function, the mean energy dissipation rate can be calculated by (Pope, 2000)

$$D_{L...L}(r) = C_n (\epsilon_{In} r)^{\zeta_n} \Leftrightarrow \epsilon_{In} = \left(\frac{D_{L...L}(r)}{C_n} \right)^{1/\zeta_n} \frac{1}{r} \, , \tag{7}$$

where C_n is a constant, e.g., $C_2 \approx 2$ (Pope, 2000), and $\zeta_n = n/3$ according to K41 by dimensional analysis. In practice, ϵ_{I2} (Table 1) is retrieved either by fitting a constant to the compensated longitudinal second-order structure function $D_{LL}(r)$, $n = 2$ in Eq. (7), or a power law ($\propto r^{2/3}$) to the inertial range of D_{LL}, defined in Eq. (A3), if the inertial range is pronounced over at least a decade. Accounting for intermittency, the scaling exponent of the nth-order structure function is modified to

7

180   $\zeta_n = \frac{n}{3}[1 - \frac{1}{6}\mu(n-3)]$ where μ is the internal intermittency exponent (Kolmogorov, 1962; Obukhov, 1962; Pope, 2000). The inertial range is bounded by the energy injection scale L at large scales and by the dissipation range at small scales. That is why the fit-range has to be chosen such that $\eta_K \ll r \ll L$. If the inertial range is not sufficiently pronounced, the extended self-similarity may be used to extend the inertial range (Benzi et al., 1993b, a). Otherwise, ϵ_{I2} can also be approximated by the maximum of Eq. (7) (for $n = 2$) within the same range as before. This is possible because the maximum lies on the plateau in

185   case of a perfect K41 inertial range scaling.

In the inertial range, the transverse second-order structure function $D_{NN}(r)$ is equal to $4D_{LL}(r)/3$ in a coordinate system where $\boldsymbol{r} = r\boldsymbol{e}_1$ is parallel to the longitudinal flow direction (Pope, 2000) highlighting the importance of the measurement direction.

2.2.3   Inertial sub-range: spectral method

190   According to K41 (Kolmogorov, 1941), the inertial sub-range of the energy spectrum function scales as $E(\kappa) \propto \langle\epsilon\rangle^{2/3}\kappa^{-5/3}$ with the wavenumber κ by dimensional analysis. In isotropic turbulence, the energy spectrum function can be converted into a one-dimensional energy spectrum $E_{11}(\kappa_1)$, see Eq. (A7). The wavenumber space is not directly accessible from one-dimensional velocity time-records. Relying on Taylor's hypothesis, the one-dimensional energy spectrum $E_{11}(\kappa_1)$ transforms to the frequency domain with $F_{11}(f) = 2\pi E_{11}(\kappa_1)/U$ where $\kappa_1 = 2\pi f/U$ (e.g., Wyngaard and Clifford, 1977; Oncley et al.,

195   1996) yielding:

$$F_{11}(f) = 18/55 C_K \left(\frac{U}{2\pi}\epsilon_S\right)^{2/3} f^{-5/3}, \tag{8}$$

which yields

$$\epsilon_S = \frac{2\pi}{U}\left(\frac{f^{5/3}F_{11}(f)}{18/55 C_K}\right)^{3/2}, \tag{9}$$

with the Kolmogorov constant $C_K = 1.5$ (Sreenivasan, 1995; Pope, 2000). Depending on the Fourier transform convention,

200   the prefactor of C_K, i.e., in the convention used here $18/55$ has to be adapted accordingly (e.g., Wyngaard, 2010). Applying Taylor's hypothesis to a flow with a randomly-sweeping mean velocity causes the Kolmogorov constant to be systematically overestimated whereas the scaling of power-law spectra remains unaffected (Wilczek and Narita, 2012; Wilczek et al., 2014). Hence, Eq. (9) is still valid for a randomly-sweeping mean velocity although ϵ_S is overestimated if C_K is not corrected for random sweeping.

205   F_{11} has the units of a power spectral density $\mathrm{m^2\,s^{-1}}$ and $\langle u_1'^2 \rangle = \int_0^\infty F_{11}(f)\mathrm{d}f$. Under the assumption of Kolmogorov scaling in the inertial sub-range, this identity can be adopted to estimate the mean energy dissipation rate from low and moderate resolution velocity measurements of a finite averaging window (Fairall et al., 1980; Siebert et al., 2006; O'Connor et al., 2010; Wacławczyk et al., 2017).

2.2.4 Energy injection scale

210   In equilibrium turbulence, the rate at which turbulent kinetic energy is transported across eddies of a given size is constant in the inertial range assuming high enough Reynolds numbers (e.g., Lumley, 1992). By a dimensional argument, this rate is proportional to $u^3(l)/l$, where $u(l)$ is the characteristic velocity scale of eddies of length l. Considering the integral scale L_{11} and its characteristic velocity scale $u(L_{11})$, namely the RMS velocity fluctuation $\sigma_{u_1'}$, the mean energy dissipation rate can be calculated by (Taylor, 1935)

215
$$\epsilon_L = C_\epsilon \frac{\sigma_{u_1'}^3}{L_{11}}, \tag{10}$$

where C_ϵ is the dissipation constant and for time- and space-varying turbulence, it depends on both initial as well as boundary conditions and the large-scale structure of the flow (Sreenivasan, 1998; Sreenivasan et al., 1995; Burattini et al., 2005; Vassilicos, 2015). C_ϵ is found to be about 0.5 for shear turbulence (Sreenivasan, 1998; Pearson et al., 2002) and 1.0 (Sreenivasan, 1984; Sreenivasan et al., 1995) or 0.73 (Sreenivasan, 1998) for grid turbulence. In this work, C_ϵ is assumed to be 0.5 which

220 holds approximately in a variety of flows (Risius et al., 2015; Sreenivasan, 1995, and references therein).

  Usually, the longitudinal integral length scale L_{11} is defined as (Pope, 2000)

$$L_{11} = \lim_{r_0 \to \infty} \int_0^{r_0} \mathrm{d}r f(r) = \frac{\pi E_{11}(0)}{2\langle u_1'^2 \rangle}, \tag{11}$$

where $f(r) = R_{11}(r)/R_{11}(0)$ is the longitudinal autocorrelation function (see also Eq. (A1) and Table A1). However, due to experimental limitations, r_0 is often given by the first zero-crossing of $f(r)$ in both laboratory and *in situ* measurements

225 (e.g., Risius et al., 2015), or, alternatively, by the position where $f(r) = 1/e$ (Tritton, 1977; Bewley et al., 2012). Griffin et al. (2019) carried out an integration for $r \to \infty$ performing an exponential fit in the vicinity of $f(r) = 1/e$. Notably, $E_{11}(0) = \int_0^\infty \mathrm{d}\kappa E(\kappa)/\kappa$ so that the estimation of L_{11} from the power spectrum is only recommended if $E(\kappa) = \frac{1}{2}\kappa^3 \frac{\mathrm{d}}{\mathrm{d}\kappa}\left(\frac{1}{\kappa}\frac{\mathrm{d}E_{11}(\kappa)}{\mathrm{d}\kappa}\right)$ (Pope, 2000) is accurately determined like in DNS. This approach not only requires a fully resolved velocity measurement but also a well converged $E_{11}(\kappa_1)$ as the conversion is highly sensitive to statistical scatter. Ultimately, the choice of L_{11} strongly

230 affects ϵ_L. In this work, we integrate $f(r)$ to the first zero-crossing because it does not depend on assumptions on the decay of $f(r)$ and the choice of the fit-range.

2.3 Simulations of homogeneous isotropic turbulence

  In this study, the direct numerical simulations of statistically homogeneous isotropic turbulent flow with $74 \leq \mathrm{R}_\lambda \leq 321$ are used as the basis for evaluating the different methods for determining the dissipation rate, see Table 2. Thereby, the performance

235 of the different methods to estimate the energy dissipation rate is not affected by violating fundamental assumptions, e.g., anisotropy or inhomogeneity. The simulations are carried out with the parallel solver TurTLE (Lalescu et al., 2022), which

solves the Navier-Stokes equations on a periodic domain using a pseudo-spectral method with a third-order Runge-Kutta time stepping. Here, we use a forcing scheme with a fixed energy injection rate on large scales.

To mimic an ensemble of single-point measurements, we introduced 1000 virtual probes into the flow (one-way coupled, i.e., without back-reaction on the flow), which move with a given constant speed in randomly-directed straight paths to record the local flow velocity. Since the trajectories of the virtual probes are randomly oriented and the probability that they are exactly aligned with the simulation boundaries is low, the effect of periodic boundaries on the recorded velocity signal is expected to be small. We assume that the virtual probe records idealized velocity time series neglecting the effect of transfer functions (e.g., Horst and Oncley, 2006; Freire et al., 2019, regarding sonic anemometry) or noise (Lenschow and Kristensen, 1985; Antonia, 2003; Lewis et al., 2021). While the root-mean-square velocity fluctuation is determined by the Navier-Stokes simulation, we can control the mean flow speed through the speed of the virtual probe. The range of used constant speeds corresponds to turbulence intensities of 1-50%. Along the trajectories, we then sample the local three-dimensional velocity field (see Fig. 1) as well as the velocity gradient field, where we use spline-interpolation to determine values in between grid points, see also (Lalescu et al., 2010, 2022). By projecting the velocity vector on the direction of the trajectory, e_1, and the orthogonal directions, e_2 and e_3, we split the velocity field in longitudinal and transverse components, respectively. From the sampled velocity gradient tensor, we compute the local instantaneous dissipation ϵ_0. The time step is limited either by the stability requirements of the flow solver or, for smaller turbulence intensities, by the required sampling frequency to capture the underlying flow. Here, we choose the time step such that the distance traveled by the probe within one step is around a tenth of the grid spacing, $U\Delta t \approx 0.1\Delta x$. The grid spacing Δx is chosen such that the highest wavenumber $k_{\max}$ satisfies $k_{\max}\eta_K \approx 3$.

Using Taylor's hypothesis, the longitudinal velocity time series correspond to at least $13L_{11}$ (for more details see Table 2) so that second- and third-order moments of both longitudinal velocity fluctuations and increments are reasonably converged (see Fig. A3). To estimate ϵ_{I3}, ϵ_{I2} and ϵ_S, the longitudinal structure functions are evaluated for scales $20\eta_K \leq r \leq 500\eta_K$ or in frequency domain for $\frac{U}{500\eta_K} \leq f \leq \frac{U}{20\eta_K}$. The ground-truth reference for the mean energy dissipation rate per virtual probe is given by $\langle\epsilon_0(\boldsymbol{x},t)\rangle_{\mathrm{VP}}$, i.e., the average of the dissipation field along the trajectory of each virtual probe. The global mean energy dissipation rate can be approximated by the ensemble average of all $\langle\epsilon_0(\boldsymbol{x},t)\rangle_{\mathrm{VP}}$ from all virtual probes, i.e., $\langle\langle\epsilon_0(\boldsymbol{x},t)\rangle_{\mathrm{VP}}\rangle_N$.

2.4 Variable Density Turbulence Tunnel (VDTT)

To evaluate the performance of different methods at Reynolds numbers applicable to atmospheric flows, we use the high-resolution hot-wire measurements of the longitudinal velocity components in the MPIDS VDTT (VDDT, Bodenschatz et al., 2014). The VDTT datasets used here are associated with $147 \leq R_\lambda \leq 5864$, which enables us to bridge the gap between DNS ($74 \leq R_\lambda \leq 321$) and atmospheric $R_\lambda \sim \mathcal{O}(10^3)$ Risius et al. (2015).

The VDTT is a recirculating wind tunnel where the working gas SF_6 is pressurized up to 15 bar to increase its density and thereby enhancing the Taylor-scale Reynolds number. To achieve the same density in air, the pressure would have had to be about 100 bar, which would have required a much thicker tunnel wall and more expensive construction. The VDTT has a horizontal length of 11.68 m and an inner diameter of 1.52 m where the rotation frequency of the fan sets the mean flow velocity ranging from 0.5 m/s to 5.5 m/s (Bodenschatz et al., 2014). Long-range correlations of the turbulent flow determine its

case id	box size	R_λ	η_K [c.u.]	I	L_{11}/η_K	$\mathcal{L}/L_{11}$
DNS 1.1	512	74	0.015	0.01	41.2	161
DNS 1.2	512	74	0.015	0.05	41.4	160
DNS 1.3	512	74	0.015	0.10	41.3	160
DNS 1.4	512	74	0.015	0.24	41.3	21
DNS 1.5	512	74	0.015	0.50	41.4	16
DNS 2.0	1024	142	0.007	0.11	99.0	332.8
DNS 2.1	1024	219	0.007	0.01	147.8	15.6
DNS 2.2	1024	217	0.007	0.06	147.6	15.7
DNS 2.3	1024	216	0.007	0.11	147.9	15.6
DNS 2.4	1024	212	0.007	0.27	146.8	15.7
DNS 2.5	1024	207	0.007	0.53	145.5	15.8
DNS 3.1	2048	302	0.003	0.01	260.9	13.6
DNS 3.2	2048	299	0.003	0.05	258.2	13.8
DNS 3.3	2048	295	0.003	0.11	254.8	14.0
DNS 3.4	2048	314	0.004	0.26	275.6	20.2
DNS 3.5	2048	321	0.004	0.53	282.9	14.7

Table 2. Parameter overview for each DNS. R_λ is the Taylor scale Reynolds number, η_K the Kolmogorov length scale, $I = \sigma_{u_1'}/U$ is the turbulence intensity, L_{11} the longitudinal integral length scale derived from $E(\kappa)$, $\mathcal{L}$ is the average probe track distance and N_p the number of virtual probes. The turbulence intensity I is controlled by setting the probe mean velocity where $\sigma_{u_1'} \approx 1$ is the root mean square longitudinal velocity fluctuation. For all cases $k_{\max}\eta_K \approx 3$, with $k_{\max}$ being the largest resolved wavenumber. For DNS 1.x and 2.x, the energy injection rate $\dot{E}_{\mathrm{in}}$ in code units is 0.4, while for DNS 3.x it is set to 0.5. The number of virtual probes N_p for DNS 1.x is 10000, whereas for DNS 2.x and DNS 3.x $N_p = 1000$.

anisotropy. These long-range correlations are shaped with the help of an active grid consisting of 111 independently rotating winglets (Küchler et al., 2019; Küchler, 2021).

Longitudinal velocity fluctuations are temporally recorded with 30 μm to 60 μm long NanoScale Thermal Anemometry Probes (NSTAP; Bailey et al., 2010; Vallikivi et al., 2011, among others) or a 450 μm long conventional hot-wire from Dantec

275 (Jørgensen, 2001) corresponding to a resolution of $< 3\eta_K$ and $< 5\eta_K$, respectively (Küchler et al., 2019) at variable distances from the active grid ranging from $\approx 6-9$ m. The velocity measurements have been extensively characterized in terms of the mean flow profiles (Küchler, 2021) as well as the decay of turbulent kinetic energy (Sinhuber et al., 2015; Sinhuber, 2015) exposing velocity probability distribution functions (PDF) being flatter than Gaussian (Küchler, 2021). The inertial-range scaling exponent ζ_2 of the longitudinal second-order structure function is in agreement with Kolmogorov's revised

280 phenomenology from 1962 ($\zeta_2 = 0.693 \pm 0.003$ for $R_\lambda > 2000$) for a large variety of wake generation schemes (Küchler et al., 2020). In the case of hot-wire measurements in the VDTT, the ground-truth energy dissipation rate for a given averaging window R is given by the gradient method $\langle \epsilon_G \rangle_R$, which converges fastest as shown in Sec. 3.5.

2.5 Strategies for the evaluation of systematic and random errors

The virtual probes record one-dimensional time records of the DNS longitudinal velocity component, from which the mean

285 energy dissipation rate can be estimated by various methods and compared with the energy dissipation rate obtained directly
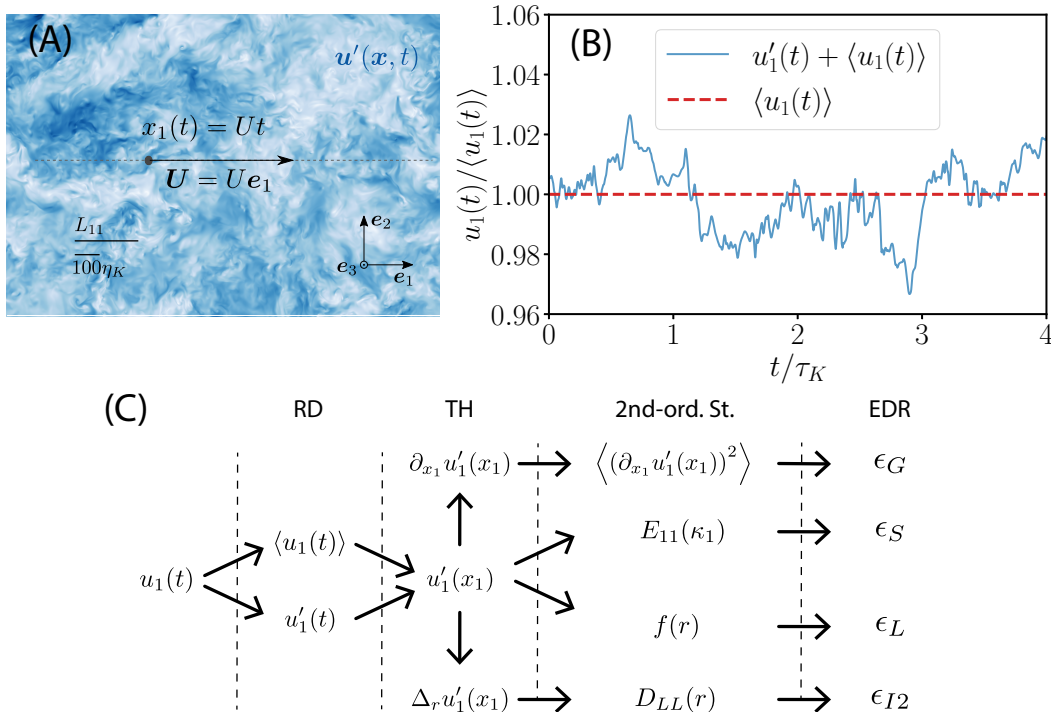
Figure 1. From single-point velocity time records to the energy dissipation rate. (A) Virtual probe sampling the three-dimensional velocity field of the DNS 3.1 (see Table 2) in time and space at a mean velocity U along its e_1-direction corresponding to turbulence intensity of 1%. (B) *One*-dimensional velocity time series $u_1(t)$ (blue solid) with corresponding time average $U = \langle u_1(t)\rangle$ (red dashed line, i.e. Eq. (1)) of the same DNS 3.1, where $u_1(t)$ is rescaled by $\langle u_1(t)\rangle$. (C) Visualization of the workflow from one-dimensional velocity time record $u_1(t)$ to the energy dissipation rate via different methods. First, $u_1(t)$ is decomposed in its mean and fluctuating part according to Reynolds decomposition (RD). Then, the velocity time series is converted into a one-dimensional velocity field invoking Taylor's hypothesis (TH). Subsequently, second-order statistics (2nd-ord. St.) of the longitudinal velocity fluctuations, its increments and first spatial derivative are inferred from which the energy dissipation rate is estimated with the help of different methods.

from the DNS dissipation field. Generally, there are two different errors when estimating the mean energy dissipation rate, namely the systematic errors and random errors. The latter is related to the estimation variance of the mean energy dissipation rate, i.e., the statistical scatter of the $\langle\epsilon\rangle_R$-estimates around the ground truth of the local mean energy dissipation rate defined in Eq. 4. The systematic error of the mean energy dissipation rate estimates expresses itself in a non-vanishing ensemble average of the deviations from the ground-truth, i.e., the global volume average defined in Eq. 5.

Systematic errors are an inherent feature of the methods used for estimating the dissipation rate, but are also affected by experimental limitations and imperfections such as averaging windows and finite turbulence intensity parameterized by R and I, respectively. One way to estimate these errors is to compare the estimated mean energy dissipation rate for a given averaging window R to the ground-truth of the DNS defined by the mean energy dissipation rate per virtual-probe track, i.e., $\langle\epsilon_0(\boldsymbol{x},t)\rangle_{\mathrm{VP},R}$. Another possibility is to compare the estimates to the ensemble average of the mean energy dissipation rate from all virtual probes, i.e., $\langle\langle\epsilon_0(\boldsymbol{x},t)\rangle_{\mathrm{VP},R}\rangle_N$, where $N = 1000$ is the total number of virtual probes. Either of these possibilities

is valid and would be interesting to understand. However, our analysis (not presented here) yields that the second approach is associated with a slightly higher value for the systematic error and a slightly higher standard deviation. For that reason, we have chosen the second approach to make a conservative assessment of the systematic errors, i.e., we compare the estimates of each method against $\langle\langle\epsilon_0(\boldsymbol{x},t)\rangle_{\text{VP},R}\rangle_N$, by

$$\beta_i = \frac{\langle\epsilon_i\rangle_R}{\langle\langle\epsilon_0(\boldsymbol{x},t)\rangle_{\text{VP},R}\rangle_N} - 1, \tag{12}$$

where $i \in \{G, I3, I2, S, L\}$ and $\langle\epsilon_i\rangle_R$ is the estimate of the energy dissipation rate via method i under the experimental limitation and imperfection such as size of averaging window or finite turbulence intensity. To distinguish between the different error terms in this manuscript, we refer to β as "reference-compared" systematic error.

In addition, the systematic error can be evaluated by comparing the estimates of the energy dissipation rate obtained by a method with imperfect data against the estimates obtained by the same method with optimal data. We denote these types of errors with δ and refer to them as "self-compared" errors. An experimental imperfection we considered here is the sensor misalignment, which is a non-zero angle of incidence θ between the longitudinal flow direction that sensor expect and U. To investigate the isolated effect of sensor misalignment, we consider a specific set of DNS with constant turbulence intensity ($I = 1\%$) and the entire track length for each virtual probe. The self-compared systematic error of each method due to misalignment is defined as

$$\delta_i(\theta) = \frac{\epsilon_i(\theta)}{\epsilon_i(0)} - 1, \tag{13}$$

where $\epsilon_i(\theta)$ is the estimate of the energy dissipation rate via method $i \in \{G, I3, I2, S, L\}$ from data with misalignment θ and $\epsilon_i(0)$ is the estimated dissipation rate from the same method and flow conditions but with an aligned sensor, i.e., $\theta = 0$.

Estimates of the mean energy dissipation rate are susceptible not only to systematic errors, but also to random errors due to statistical uncertainty. For the averaging window, errors given by Eq. (12) would be the best indicator of systematic errors. However, random errors due to size of averaging window can also be significant. When the spatial averaging window R (or temporal averaging window τ) is finite, we capture the self-compared random error for each individual method by

$$\delta_i(R) = \sqrt{\left\langle \left(\frac{\langle\epsilon_i\rangle_R}{\langle\langle\epsilon_i\rangle_R\rangle_N} - 1 \right)^2 \right\rangle_N}, \tag{14}$$

where $\langle\epsilon_i\rangle_R$ is the local mean energy dissipation rate based on the averaging window R normalised by its ensemble average, i.e., $\langle\langle\epsilon_i\rangle_R\rangle_N$. Eq. (14) indeed calculates the standard deviation of the normalized $\langle\epsilon_i\rangle_R$, which is used here as a proxy for the random error. Table 3 provides an overview of the different error types and terminologies used here.

Symbol	Definition	Equation
β_i	reference-compared systematic error, i.e., relative to ground-truth reference $\langle\langle\epsilon_0(\boldsymbol{x},t)\rangle_R\rangle_N$	(12)
$\delta_i(\theta)$	self-compared (systematic) error of each method at a given misalignment angle θ relative to the estimates provided by the same method but at $\theta = 0$	(13)
$\delta_i(R)$	self-compared (random) error at a given averaging window of R or τ relative to the average value from all virtual probes at the same averaging window of R or τ	(14)

Table 3. Different types of errors investigated in this study and their definitions. $i \in \{G, I3, I2, S, L\}$, where G stands for gradient method, $I3$ for 4/5 law, $I2$ for second-order structure function in the inertial range, S for the spectral method, and L for the scaling argument. The averaging window is denoted spatially by R and temporally by τ. The misalignment angle is represented by θ.

3 Results and Discussion

In the following, we first focus on the DNS data to calculate $\epsilon_G, \epsilon_{I3}, \epsilon_{I2}, \epsilon_S$, and ϵ_L from the entire longitudinal velocity time records of all virtual probes and compare these estimates against the ground-truth reference. Then, we systematically investigate the impact of turbulence intensity, (virtual) probe orientation, and averaging window size for all methods of interest. The influence of flow Reynolds number on the presented results are then discussed by taking into account the VDTT data together with the DNS data. Finally, we provide a proof of concept for a time-dependent dissipation rate calculation by comparing the dissipation time series measured by ϵ_G, ϵ_{I2}, and ϵ_L and its coarse-grained surrogate. In the following, we use the definitions of systematic and random errors as mentioned in Sec. 2.5 and Table 3.

3.1 Verification of the analytical methods and a first insight into their performance under ideal conditions

To verify the implementation of our methods, only data from cases with a low turbulence intensity of 0.01 and an averaging window covering the entire size of the probe track are used in this section. Furthermore, ϵ_{I2} and ϵ_{I3} are obtained by a fit according to Eq. (7) with $n = 2$ and $n = 3$, respectively, in the inertial range with $r \in [20\eta_K, 500\eta_K]$ for DNS 2.1 and 3.1. Analogously, ϵ_S is inferred from the inertial range fit, Eq. (9), in the range $f \in [U/(500\eta_K), U/(20\eta_K)]$. For DNS 1.1 with $R_\lambda = 74$, due to the absence of an inertial range for low Taylor-scale Reynolds number (see Fig. A7), the maximum of Eq. (7) is used to infer ϵ_{I2} and ϵ_{I3} instead of fitting the inertial range.

β errors	mean [%]	median [%]	std. dev. [%]	range [%]
β_{ref}	0.0	-0.7	18.6	-49.8...68.2
β_G	-0.5	-1.7	19.3	-48.1...75.4
β_{I2}	8.8	3.1	41.7	-69.6...199.8
β_{I3}	49.2	10.1	123.1	-93.1...822.2
β_S	4.1	-2.0	32.1	-55.2...210.4
β_L	40.0	31.5	59.6	-69.5...352.9

Table 4. Statistics (mean, median, standard deviation and range) of the reference-compared systematic errors for different methods and case DNS 3.1 with $R_\lambda = 302$. Here β_{ref} is defined as $= \langle\epsilon_0(\boldsymbol{x},t)\rangle_{\text{VP}}/\langle\langle\epsilon_0(\boldsymbol{x},t)\rangle_{\text{VP}}\rangle_N - 1$, which shows the actual variability in the dissipation rate field. The last column shows the range of minimum to maximum percentage deviation from the mean.
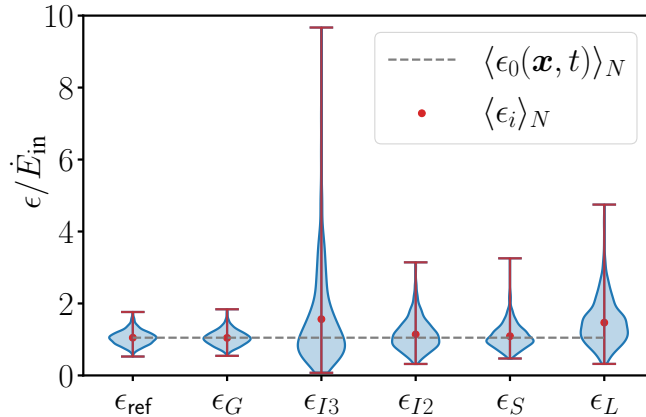
Figure 2. Validation of estimating the energy dissipation rate from $\epsilon_G, \epsilon_{I2}, \epsilon_{I3}, \epsilon_S,$ and ϵ_L re-scaled by the energy injection rate $\dot{E}_{\mathrm{in}}$. The data are taken from DNS 3.1 with 1000 probes, $R_\lambda = 302$, $I = 1\%$, $\theta = 0°$ and maximal available averaging window ($R \approx 3550\eta_K$). The ensemble mean of each method $\langle \epsilon_i \rangle_N$ is denoted by red dots where the whiskers extend from the minimal to maximal estimate of ϵ_i where $i \in \{G, I3, I2, S, L\}$. The reference mean energy dissipation rate for each probe is given by ϵ_{ref}. The dashed line represents the re-scaled global mean energy dissipation rate of DNS 3.1 which is approximated by the ensemble average of the true mean energy dissipation rate along the trajectory of each virtual probe.

The distribution of the mean energy dissipation rate estimated by $\epsilon_G, \epsilon_{I2}, \epsilon_{I3}, \epsilon_S,$ and ϵ_L for each probe at $R_\lambda = 302$ is shown in Fig. 2 and Table 4. Estimations for other R_λ are shown in supplementary Fig. A1. The best performing method is the gradient

340   method ϵ_G with the range being also very close to the range of β_{ref}, where as ϵ_{I3} is associated with the mean highest deviation. The superior performance of ϵ_G compared to others is mainly due to the fact that it relies on (dissipation-range) second-order statistics that can be captured with fast statistical convergence within a short sampling interval. Hence, the distribution of ϵ_G and ϵ_{ref} are similar. ϵ_{I3}, on the other hand, relies on third-order moments of the velocity increments of inertial scales associated with slower statistical convergence compared to ϵ_G. Therefore, ϵ_{I3} requires longer velocity records than ϵ_G to converge under

345   stationary conditions. For this reason, the third-order structure function is not considered further in this study, as one of the main objectives of this study is to evaluate different methods suitable for extracting the time-dependent energy dissipation rate.

Figure 2 and Table 4 also shows that the estimates of the energy dissipation rate provided by $D_{LL}(r)$ and $E_{11}(\kappa_1)$ are close to each other, which can be explained by the fact that they are both second-order quantities (in real and Fourier space, respectively) connected by $f(r)$. Unlike ϵ_G, both ϵ_{I2} and to a lesser extent ϵ_S tend to overestimate the energy dissipation

350   rate. However, ϵ_S depends much stronger on properly setting the fit-range than ϵ_{I2} (supplementary Fig. A2). The spectral method ϵ_S can differ by a factor of 2 from ϵ_{I2} depending on the high-frequency limit. This factor of 2 is in accordance with a comparison of ϵ_{I2} and ϵ_S by a linear fit resulting in a slope close to 0.5 (Akinlabi et al., 2019). In the DNS, the power spectrum is subject to strong statistical uncertainty at high frequencies without ensemble-averaging the spectra of each virtual probe or longer DNS runtimes. As the high-frequency limit of the inertial range of the spectrum is hardly distinguishable

355   from its dissipation range, the choice of the fit-range range for ϵ_S is related to the fit-range of the longitudinal second-order structure function by $f \in [U/(500\eta_K), U/(20\eta_K)]$ as mentioned above. Wacławczyk et al. (2020) found that the estimation of

15

the energy dissipation rate from the power spectral density is generally robust at small wavenumbers (i.e. larger length scales) whereas the second-order structure function performs better at small length scales (i.e. larger wavenumbers). With our choice of the fit-range $r \in [20\eta_K, 500\eta_K]$ for DNS 3.1 dataset shown in Fig. 2, we confirm that ϵ_{I2} is already reliable at the lower end of the inertial range where dissipative effects are negligible.

At last, ϵ_L overestimates by 40% on average, this systematic overestimation might be due to the difficulty in determining L_{11} as different methods for estimating the integral length L_{11} can contribute to the systematic bias of ϵ_L. As mentioned above, we infer the longitudinal integral length from fitting $f(r)$ to the first zero crossing which yields, at least in the DNS of this work, a systematic underestimation due to the scatter in both $\sigma_{u_1'}$ and L_{11}, as illustrated in Fig. A3 and A4. However, the accuracy of the dissipation constant C_ϵ, which is a function of large-scale forcing and initial conditions (Vassilicos, 2015; Sreenivasan, 1998; Sreenivasan et al., 1995; Burattini et al., 2005), can potentially cause larger mean deviations. Advantageously, the large-scale estimate ϵ_L is applicable to low-resolution measurement. Figure A1 and Table A3 gives an overview of the systematic errors of the different methods at different Reynolds numbers, showing that the above conclusions are also valid for lower R_λ.

3.2 Validity of Taylor's hypothesis and impact of random sweeping effects

For a large turbulence intensity the local speed and direction of the flow is significantly varying in time and space, which hinders the applicability of the Taylor's hypothesis. Here, we quantify the impact of random sweeping on the accuracy of determining the mean energy dissipation rate. Therefore, we set the mean speed of the virtual probes in each DNS so that the turbulence intensity, and in consequence the random sweeping, is a control parameter.

Figure 3 shows the systematic errors β_i for ϵ_G, ϵ_{I2}, ϵ_S, and ϵ_L at different turbulence intensities for DNS 3.1-5. For each virtual probe taken into account in Fig. 3, we used the entire time series so that the size of the averaging window is maximal. While each method has a different systematic error and scatter, Fig. 3 indicates that the mean relative deviation of each estimate from the global mean $\langle\langle\epsilon_0(\boldsymbol{x}, t)\rangle_{\mathrm{VP}}\rangle_N$ increases with turbulence intensity. This is particularly strong for the gradient method. For $I = 1\%$ and $I = 10\%$, the gradient method has the lowest scatter in terms of the standard deviation σ_{β_G} (19.3% and 27.3%) and the lowest systematic error in terms of the $\langle\beta_G\rangle_N$ (-0.5% and 6.1%), respectively. At higher turbulence intensities, ϵ_{I2} is the least affected method with $\langle\beta_{I2}\rangle_N = 6.5\%$ and $\sigma_{\beta_{I2}} = 37.2\%$ for $I = 25\%$ as well as $\langle\beta_{I2}\rangle_N = 24.5\%$ and $\sigma_{\beta_{I2}} = 56.9\%$ for $I = 50\%$. At the highest turbulence intensities, both ϵ_L and ϵ_S are associated with lower mean β than that of ϵ_G.

The fraction of track samples that can lead to a deviation of larger than 100% increases from 0% to $\sim 60\%$ for ϵ_G as the turbulence intensity increases from 1% to 50%. We hypothesize that these deviations of the mean are the result of random sweeping effects, which limit the applicability of Taylor's hypothesis. In frequency space, Taylor's hypothesis (Taylor, 1938) establishes a one-to-one mapping between the frequency and the streamwise wavenumber, i.e., $\omega = \kappa_1 U$. As the turbulence intensity grows, a randomly sweeping mean velocity smears out this correspondence between frequencies and wavenumbers. For the spectrum, this smearing out effectively moves energy from larger scales to smaller and less energetic ones (Lumley, 1965; Tennekes, 1975). Therefore, it leads to an overestimation in the inertial and dissipation range of the spectrum, thus, affecting the inertial range and gradient method. To visualize this overestimation, we evaluate the effect of random sweeping on the spectrum (Eq. (B2)) numerically for different turbulence intensities at the example of a model spectrum (Eq. (B4)). The

result is shown in Fig. 4, where the spectrum is pre-multiplied by κ_1^2 to later highlight the effect on the gradient method. Here, the overestimation is most pronounced in the dissipative range.
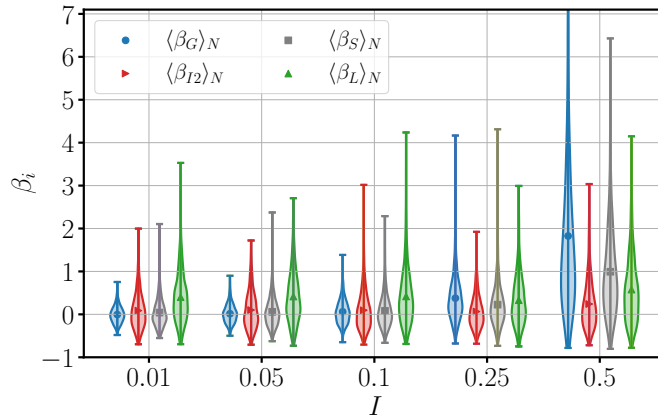
Figure 3. Systematic error β_i, Eq. (12), as a function of turbulence intensity $I \in \{0.01, 0.05, 0.1, 0.25, 0.5\}$ for ϵ_G (●), ϵ_{I2} (►), ϵ_S (■), and ϵ_L (▲). The energy dissipation rates are estimated from each longitudinal velocity time series of DNS 3.1-5 with ideal alignment ($\theta = 0°$) where the maximal available window size was used. The fit-range for the inertial range of the power spectral density is chosen to be within $U/(500\eta_K) \leq f \leq U/(20\eta_K)$ where η_K is the Kolmogorov length scale, and, equivalently in space domain, $20\eta_K \leq r \leq 500\eta_K$ for the longitudinal second-order structure function. The upper limit of the y-axis is chosen to be 7.1 for improving the plot visibility (there are some outliers of ϵ_G for $I = 50\%$).

To quantify the impact of random sweeping on estimates of $\langle\epsilon\rangle$, we first consider the influence of random sweeping on the gradient method. For the gradient method, Lumley (1965) and Wyngaard and Clifford (1977) have shown that in isotropic turbulence random sweeping leads to an relative deviation of the volume-averaged mean energy dissipation rate by

$$\frac{\epsilon_G}{\langle\epsilon\rangle} - 1 = \beta_G = 5I^2 \quad \text{with} \quad \epsilon_G = 15\nu \int \kappa_1^2 E_{11}(\kappa_1) d\kappa_1 = \langle\epsilon\rangle[1 + 5I^2]. \tag{15}$$

We illustrate this result in the appendix Sec. B, where we consider a model wavenumber-frequency spectrum (Wilczek and Narita, 2012; Wilczek et al., 2014), which is based on the same modeling assumptions used in Wyngaard and Clifford (1977). Due to the κ_1^2-weighting of the gradient method, the mean dissipation rate estimate is highly sensitive to the viscous cutoff of the energy spectrum, which is overestimated by random sweeping effects, see Fig. 4. As a consequence, deviations of the estimated dissipation rate are growing rapidly with turbulence intensity. In the right panel of Fig. 4, we compare the effect of random sweeping on the gradient method obtained with a model spectrum, the one computed by Lumley (1965), and the observed deviations by measurements of the virtual probes in a DNS flow; here shown are the DNS 3.1-5. In fact, the estimate from Lumley (1965) can explain the magnitude of deviations observed by the virtual probes in case of ϵ_G up to $I = 25\%$. The strong deviation of β_G at $I = 50\%$ is likely due to the sensitivity of the gradients on the space-to-time conversion via Taylor's hypothesis: at high turbulence intensities, the mean velocity becomes smaller compared to the fluctuations. Therefore, the error of estimating the mean velocity due to finite averaging window, Eq. (2), increases relative to the mean velocity. Larger relative errors in the estimated mean velocity lead - applying Taylor's hypothesis - to both under- and overestimated

17

spatial gradients for the individual averaging windows, additional to the effect of random sweeping. Similarly this results in an additional overestimation of the dissipation rate. These deviations do not appear in evaluating random sweeping effects based on a model spectrum as there the mean velocity is a parameter we choose.

Now let us consider the two inertial sub-range methods. Here, as one can see in Fig. 3 and 4, the increase of the mean relative deviation, β_i, is less pronounced. In the inertial sub-range, random sweeping causes an overestimation of the spectrum of merely several percent while the inertial range scaling is preserved as shown in Wyngaard and Clifford (1977); Wilczek et al. (2014). As both the second-order structure function and the spectral method are based on the inertial sub-range of the energy spectrum, the effect of a randomly sweeping mean velocity is expected to be small on ϵ_{I2} and ϵ_S. Here, the overestimation of the spectrum can be used to express the relative systematic deviation of both ϵ_{I2} and ϵ_S for different turbulence intensities analytically:

$$\frac{\epsilon_{I2/S}}{\langle \epsilon \rangle} - 1 = \beta_{I2/S} = (C_T(I))^{3/2} - 1 \quad \text{with} \quad C_T(I) = \frac{5}{6} \int\limits_0^\infty \left[\text{erf}\left(\frac{y+1}{\sqrt{2}I} \right) - \text{erf}\left(\frac{y-1}{\sqrt{2}I} \right) \right] y^{2/3} \, \mathrm{d}y, \tag{16}$$

where $C_T(I)$ quantifies the spectral overestimation as function of mean wind and fluctuations defined as in (Wilczek et al., 2014). In Fig. 4B we compare the observed deviations from the DNS to Eq. (16). This shows that Eq. (16) underestimates β_{I2} for $I \in \{0.01, 0.05, 0.1\}$ (i.e. DNS 3.1, 3.2 and 3.3). The underestimation is most likely due to additional random errors associated with finite averaging window lengths. It is obvious from Table 2 that DNS 3.3 has statistically the shortest probe tracks $\sim 3440\eta_K$ (DNS 3.1: $\sim 3550\eta_K$, DNS 3.2: $\sim 3560\eta_K$). Nonetheless, β_{I2} matches the prediction of Eq. (16) for $I \in \{0.25, 0.5\}$ where the corresponding probe tracks statistically amount to $\sim 5570\eta_K$ and $\sim 4260\eta_K$, respectively. The effect of the averaging window size on ϵ_{I2} is explored in Sec. 3.4. We conclude that Eq. (16) can be used to estimate the error introduced by random sweeping of ϵ_{I2}.

For the spectral method, Eq. (16) underestimates the relative error β_S for all turbulence intensities. This may be due to the strong dependence of ϵ_S on the U-based fitting range, i.e., $f \in [U/(500\eta_K), U/(20\eta_K)]$, which can differ significantly between virtual probes at high turbulence intensities. Further work is needed to assess the dependence of the spectral method on the choice of the fit-range for finite turbulence intensities.

Overall, random sweeping effects explain why the gradient method is more sensitive to turbulence intensity than inertial-range methods. Here, random sweeping accurately captures the deviations of the second-order structure function method as a function of turbulence intensity whereas it can only partially account for the observed deviations for the spectral method.

3.3 Probe Misalignment

In this section, we assess the influence of probe misalignment with respect to the mean flow direction on estimating the energy dissipation rate at the energy injection scale, the inertial range and the dissipation range. Here, we assume the angle θ between the (virtual) anemometer and the global mean wind direction $\frac{U}{|U|}$ to be constant throughout the sampling trajectory. As it can be seen from Eq. (C5), ϵ_L depends on θ. Then, the analytically derived error for ϵ_L due to misalignment of the sensor and the

18
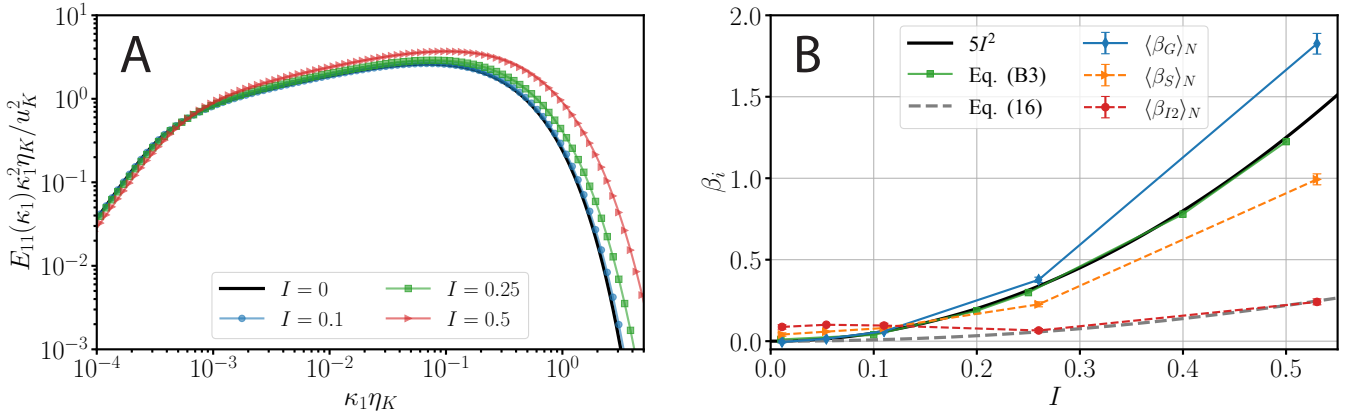
Figure 4. The effects of random sweeping on the energy dissipation estimates. (A) Premultiplied model energy spectrum with random sweeping effects, Eq. (B2), for turbulence intensities $I \in \{0.1, 0.25, 0.5\}$ where the original energy spectrum corresponds to $I = 0$. In Eq. (B4), $\langle \epsilon \rangle$ is chosen to be equal to 1 $\mathrm{m^2 s^{-3}}$, the Kolmogorov length scale to $\eta_K \approx 0.00038$ m. $u_K = (\nu \langle \epsilon \rangle)^{1/2}$ is the Kolmogorov velocity scale. (B) Systematic over-prediction illustrated by the relative error β_i, Eq. (12), at different turbulence intensities. The systematic over-prediction by (Lumley, 1965) (solid black) matches with the numerically obtained systematic error β_G for the gradient method relative to the ground-truth reference $\langle \epsilon \rangle$ by using the model spectrum (Eq. (B3), green squares). Both reasonably estimate the data obtained from DNS 3.1-5 (blue diamonds) up to a turbulence intensity of $I = 25\%$. Also, we show the systematic over-prediction of inertial sub-range methods (β_S: orange triangles, and β_{I2}: red circles, both from Eq. (12)) compared to the analytically derived error obtained by the random sweeping model ($\beta_{I2,S}$, Eq. (16), grey dashed).

440 longitudinal wind direction is given by

$$\delta_L(\theta) = \frac{\epsilon_L(\theta)}{\epsilon_L(0)} - 1 = \frac{2}{\cos\theta(1 + \cos^2\theta)} - 1, \tag{17}$$

where $\epsilon_L(\theta)$ represents the energy dissipation that is derived given an angle of incidence θ and $\epsilon_L(0)$ is the reference value for perfect alignment of the mean flow direction and the probe, i.e., when $\theta = 0$.

Analogously, the second-order structure function tensor is affected by misalignment (cf. appendix C). Thus, it can be shown

445 that the analytically derived error $\delta_{I2}(\theta)$ as a function of θ reads

$$\delta_{I2}(\theta) = \frac{\epsilon_{I2}(\theta)}{\epsilon_{I2}(0)} - 1 = \left(\frac{4 - \cos^2\theta}{3} \right)^{3/2} \frac{1}{\cos\theta} - 1, \tag{18}$$

where $\epsilon_{I2}(\theta)$ represents the energy dissipation that is derived given an angle of incidence θ and $\epsilon_{I2}(0)$ is the reference value for perfect alignment of the mean flow direction and the probe. As outlined in Appendix C and with Eq. (5), the analytically derived error of ϵ_G as a function of θ can be calculated to

450
$$\delta_G(\theta) = \frac{\epsilon_G(\theta)}{\epsilon_G(0)} - 1 = 2 \left(\frac{1}{\cos^2\theta} - 1 \right), \tag{19}$$

19
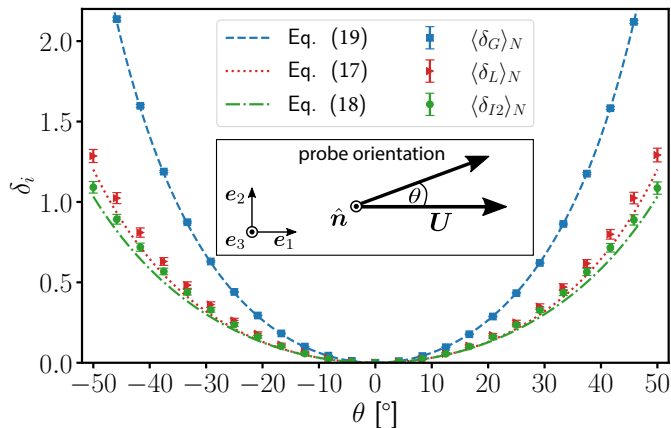
Figure 5. Influence of misalignment between probe orientation and the mean flow direction U in terms of the average error of the energy dissipation rate $\delta_i(\theta)$ as a function of the angle of attack θ. The energy dissipation rates are derived from DNS 3.1 with a turbulence intensity of 1%, $R_\lambda = 293$ and maximally available window size. The error bars are given by the standard error of the mean. The analytically derived errors $\delta_L(\theta)$, $\delta_{I2}(\theta)$ and $\delta_G(\theta)$ are given by Eqs. (17), (18) and (19) respectively. The ordinate is limited from 0 to 2.2 to guarantee a better visibility for $\delta_L(\theta)$ and $\delta_{I2}(\theta)$. The inset visualizes the misalignment angle θ between the probe orientation and the mean flow direction U. The rotation axis is denoted by $\hat{n}$. As mentioned above, the mean flow direction U is considered as the longitudinal direction of the flow.

where $\epsilon_G(\theta)$ represents the energy dissipation that is derived given an angle of incidence θ and $\epsilon_G(0)$ is the reference value for perfect alignment of the mean flow direction and the probe.

To compare the analytical expressions to DNS results, the sensing orientation of the virtual probes is rotated around the e_3-axis in the coordinate system of each the virtual probe by an angle θ relative to their direction of motion, i.e., the e_1-axis. Then, $\epsilon_L(\theta)$, $\epsilon_{I2}(\theta)$, and $\epsilon_G(\theta)$ are inferred from the new longitudinal velocity component. The ensemble-averaged relative errors of the estimated energy dissipation rates $\delta(\theta)$ due to misalignment is shown as a function of θ in Fig. 5 in the range of $\pm 50°$ both for DNS and the analytically derived Eqs. (19), (17), and (18). In general, the ensemble-averaged systematic errors follow the analytically derived errors reliably in terms of the limits of accuracy for all R_λ at turbulence intensity $I = 1\%$. The longitudinal second-order structure function is the best performing method with a systematic error $\langle \delta_{I2} \rangle_N$ of lower than 20% for $\theta \in [-25°, 25°]$, which increase to 100% at $\theta = \pm 50°$. $\langle \delta_L \rangle_N$ is similarly affected by misalignment but slightly larger than $\langle \delta_{I2} \rangle_N$. Despite its rapid statistical convergence, ϵ_G is the most vulnerable method by misalignment compared to the other two methods.

In experiments where the sensor can be aligned to the mean wind direction within $\theta \in [-10°, 10°]$ over the entire record time, $\delta_i(\theta)$ is expected to be small. Further work is needed to evaluate the impact of a time-dependent misalignment angle $\theta(t)$. We suppose that keeping the angle of attack θ fixed over the entire averaging window, here the entire time record of each probe, potentially leads to overestimation of $\delta_i(\theta)$ with θ being a function of time in practice.

3.4 Systematic errors due to finite averaging window size R

Here, our goal is to investigate how the accuracy of estimating the global mean energy dissipation rate depends on the averaging window size by investigating the associated systematic and random errors individually. To do this, we select an averaging window of size R from the beginning of each track of virtual probes for case DNS 3.1. In this way, we obtain 1 subrecord for each virtual probe, which amounts to a total of 1000 subrecords for each averaging window R. From each of these subrecords a mean value of ϵ_0 (i.e. $\langle\epsilon_0(\boldsymbol{x},t)\rangle_{\mathrm{VP},R}$), $\langle\epsilon_G\rangle_R$, $\langle\epsilon_L\rangle_R$ and $\langle\epsilon_{I2}\rangle_R$ is then evaluated. The smallest R considered for these analyses is $501\eta_K$, which is limited by the upper bound of the fitting range $r \in [20\eta_K, 500\eta_K]$ for estimating ϵ_{I2}. The largest window size considered in this section is $3000\eta_K$, which is limited by the total length of the virtual-probe track (Table 2).

Before comparing estimates of the energy dispersion rate using different methods, let us first compare the locally averaged energy dispersion rate $\langle\epsilon_0(\boldsymbol{x},t)\rangle_{\mathrm{VP},R}$ with the instantaneous energy dispersion rate, which is shown in Fig. 6A. All averaging window sizes create PDFs with similar shape, but significantly different from the shape of the instantaneous field. The larger the volume over which the dissipation field is averaged, the more the $\mathrm{PDF}(\langle\epsilon_0(\boldsymbol{x},t)\rangle_{\mathrm{VP},R})$ converges to a peak at the global mean energy dissipation rate normalised by $\dot{E}_{\mathrm{in}}$, i.e. $\langle\epsilon_0(\boldsymbol{x},t)\rangle/\dot{E}_{\mathrm{in}} \approx 1.0$.

We can further explore the influence of averaging window R for each method by examining the distribution of systematic errors, i.e., β_i, as shown in Fig. 6B-D. The first main point to note is the fact that all methods at small R tend to peak at a dissipation rate lower than the global. Hence, the mean energy dissipation rate is most likely underestimated. All $\mathrm{PDF}(\beta_i(R))$ become narrower and the mean relative errors $\beta_i(R)$ converge to 0 as R increases. The second main point to consider is the statistical uncertainty, causing a random error in estimating the local mean energy dissipation rate $\langle\epsilon_0(\boldsymbol{x},t)\rangle_{\mathrm{VP},R}$. As it can be seen in Fig. 6B-D, the width of the distribution is wide with asymmetric long tails, especially for β_{I2} and β_L. This is an indication that high random errors are to be expected in the estimation of the mean energy distribution rate.

3.5 Random errors due to finite averaging window size R

We now focus on random errors associated with ϵ_G, ϵ_L and ϵ_{I2} analytically. We denote $\langle\epsilon_G\rangle_R$, $\langle\epsilon_L\rangle_R$ and $\langle\epsilon_{I2}\rangle_R$ the energy dissipation rates that are estimated for a longitudinal velocity time record for a window of size R. For the calculation of random errors caused by the choice of the size of the averaging window, we consider DNS 1.3, 2.3, and 3.3, as well as wind tunnel experiments that all have a comparable turbulence intensity of $I \approx 10\%$.

Both the second-order structure function, Eq. (A3), and the scaling argument, Eq. (10), depend on the variance $\langle u_1'^2\rangle$ of the longitudinal velocity time record. ϵ_G is also related to $\langle u_1'^2\rangle$ through Eqs. (6) and (A1). The variance $\langle u_1'^2\rangle$ itself is subject to both systematic and random errors in case of a finite averaging window $R < \infty$. Assuming an ergodic, hence, a stationary velocity-fluctuation time-record with a vanishing mean, the systematic error in estimating the variance over an averaging window of size R is given by (following Lenschow et al., 1994, while applying Taylor's hypothesis)

$$\Delta_{\langle u_1'^2\rangle} = \left\langle \frac{\langle u_1'^2\rangle_R}{\langle u_1'^2\rangle} - 1 \right\rangle_N \approx -2\frac{L_{11}}{R}, \tag{20}$$
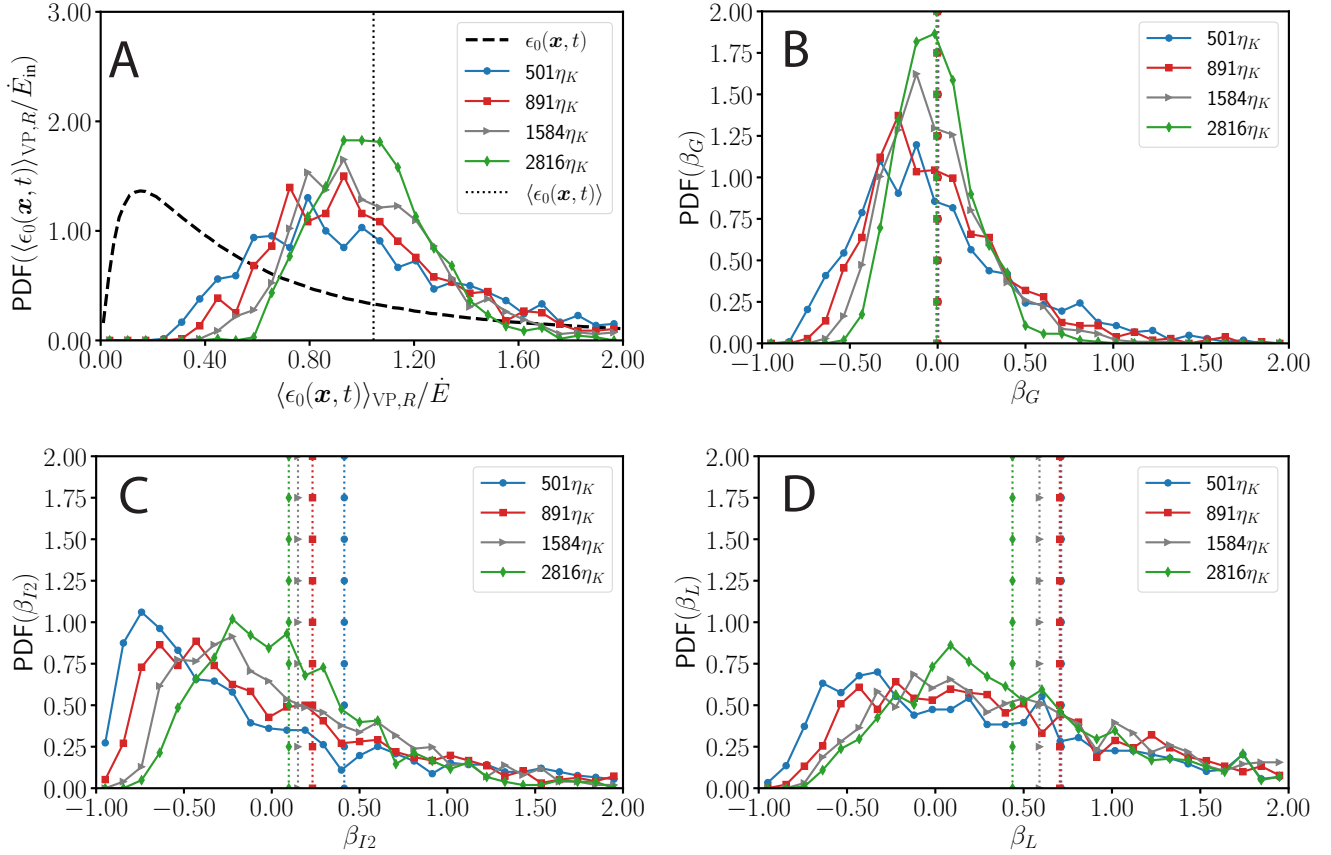
Figure 6. The effect of the averaging window size R (A) on the distribution of $\langle \epsilon_0(\boldsymbol{x},t) \rangle_{\mathrm{VP},R} / \dot{E}_{\mathrm{in}}$; and on the accuracy of estimates obtained via (B) $\langle \epsilon_G \rangle_R$, (C) $\langle \epsilon_{I2} \rangle_R$, and (D) $\langle \epsilon_L \rangle_R$ in terms of the systematic errors β_G, β_{I2}, and β_L, respectively, from the ground-truth reference $\langle \epsilon_0(\boldsymbol{x},t) \rangle_{\mathrm{VP},R}$ as given by Eq. (12). The velocity time records of the longitudinal component are taken from DNS 3.1 ($\mathrm{R}_\lambda = 302$, $I = 1\%$, $\theta = 0°$). In (A), the distribution of the instantaneous dissipation rate $\epsilon_0(\boldsymbol{x},t) / \dot{E}_{\mathrm{in}}$ sampled by all virtual probes is shown by the dashed line, and the global average energy dissipation rate normalized by $\dot{E}_{\mathrm{in}}$ is shown by the dotted vertical line. The other PDFs in A are from the local average of the energy dissipation rate obtained from a window of size R at the beginning of each virtual probe, i.e., 1000 averaged values for a given R. In (B), (C) and (D) the vertical dotted lines correspond to ensemble averages of the systematic errors β_i. The ensemble average of β_G slightly decreases from 0.4% for $R = 501\eta_K$ to -0.7% for $R = 2815\eta_K$ where the standard deviation of β_G decreases from 50% to 22%. The ensemble average of β_{I2} decreases from 41% to 10% and the standard deviation from 185% to 5%. β_L exhibits stronger deviations (mean β_L of $\sim 44\%$ and standard deviation $\sim 67\%$ for $R = 2816\eta_K$).

where $\langle u_1'^2 \rangle_R$ is the estimated variance based on the (finite) averaging window R, $\langle u_1'^2 \rangle$ is the true variance and it is assumed $R \gg L_{11}$. The always negative error predicted by Eq. (20) indicates that, for finite averaging window sizes, the variance $\langle u_1'^2 \rangle$ is always statistically underestimated, which agrees with Fig. A3A. Eq. (20) furthermore indicates that the systematic error of the variance estimates can be neglected for *sufficiently* long averaging windows $R \gg L_{11}$.

The variance estimates are also subject to statistical uncertainty, which is also known as the random error of variance estimation (Lenschow et al., 1994). Assuming that $u_1'(t)$, which has a zero mean, can be modeled by a stationary Gaussian process and that its autocorrelation function is sufficiently well represented by an exponential, the random error of estimating the variance can be expressed as (following Lenschow et al., 1994, while applying Taylor's hypothesis)

$$e_{\mathrm{rand}} = \sqrt{\left\langle \left(\frac{\langle u_1'^2 \rangle_R - \langle\langle u_1'^2 \rangle_R \rangle_N}{\langle u_1'^2 \rangle} \right)^2 \right\rangle_N} \approx \sqrt{\left\langle \left(\frac{\langle u_1'^2 \rangle_R}{\langle\langle u_1'^2 \rangle_R \rangle_N} - 1 \right)^2 \right\rangle_N} \approx \sqrt{\frac{2L_{11}}{R}} , \tag{21}$$

where it is assumed $R \gg L_{11}$ such that the systematic error can be neglected and, hence, $\langle\langle u_1'^2 \rangle_R \rangle_N \approx \langle u_1'^2 \rangle$. Here, $\langle\langle u_1'^2 \rangle_R \rangle_N$ is the ensemble average of the variance estimates $\langle u_1'^2 \rangle_R$ for an averaging window R. It can be seen that e_{rand} is larger than the systematic error, (20), when $R > L_{11}$.

Consequently, the estimation of the mean energy dissipation rate by the scaling argument, Eq. (10), is affected by the (absolute) random error of the variance estimation given by the product of e_{rand} and $\langle\langle u_1'^2 \rangle_R \rangle_N$. Invoking the Gaussian error propagation, the analytically derived error reads

$$\delta_L(R) = \frac{1}{\langle \epsilon_L \rangle_R} \frac{\partial \langle \epsilon_L \rangle_R}{\partial \langle u_1'^2 \rangle_R} \underbrace{\underbrace{e_{\mathrm{rand}}}_{\text{relative random error of } \langle u_1'^2 \rangle_R} \langle\langle u_1'^2 \rangle_R \rangle_N}_{\text{absolute random error of } \langle u_1'^2 \rangle_R} = \frac{3}{2} \sqrt{\frac{2L_{11}}{R}} , \tag{22}$$

where e_{rand} is the relative random error of the variance estimate of the velocity fluctuations $\langle u_1'^2 \rangle_R$ defined in Eq. (21), and $\langle u_1'^2 \rangle_R$ is the variance estimate of u_1' based on the averaging window R. Then, the absolute random error of the variance estimate of the velocity fluctuations $\langle u_1'^2 \rangle_R$ is given by $e_{\mathrm{rand}} \langle u_1'^2 \rangle_R$. $\delta_L(R)$ is a relative error itself, hence the prefactor $1/\langle \epsilon_L \rangle_R$. Notably, $\delta_L(R)$ scales as $R^{-1/2}$.

Similarly, the longitudinal second-order structure function is also affected by the estimation variance of the variance,

$$e_{D_{LL}} = \sqrt{\left\langle \left(\frac{D_{LL}(r;R)}{\langle D_{LL}(r;R) \rangle_N} - 1 \right)^2 \right\rangle_N} = \sqrt{\left\langle \left(\frac{2\langle u_1'^2 \rangle_R (1 - f(r))}{2\langle\langle u_1'^2 \rangle_R \rangle_N (1 - f(r))} - 1 \right)^2 \right\rangle_N} \approx \sqrt{\frac{2L_{11}}{R}} , \tag{23}$$

where $D_{LL}(r;R)$ is the longitudinal second-order structure function evaluated over an averaging window of size R and under the assumption that the longitudinal auto-correlation function $f(r)$ is *sufficiently* converged over the range of the averaging window. This is a simplistic assumption that may be questionable in some cases, but a more robust evaluation of the validity of the assumption is complex and beyond the scope of this study.

Thus, the uncertainty of estimating the variance propagates to $\langle \epsilon_{I2} \rangle_R$ relying on $D_{LL}(r; R)$ (Eq. (7) for $n = 2$). The random error $\delta_{I2}(R)$ can be analytically inferred from the random error of the second-order structure function $\sigma_{D_{LL}}$ by Gaussian error propagation yielding

$$\delta_{I2}(R) = \frac{1}{\langle \epsilon_{I2} \rangle_R} \frac{\partial \langle \epsilon_{I2} \rangle_R}{\partial D_{LL}} e_{D_{LL}} \langle D_{LL}(r; R) \rangle_N = \frac{3}{2} \sqrt{\frac{2L_{11}}{R}}, \tag{24}$$

which shows that $\delta_{I2}(R)$ scales as $R^{-1/2}$ similar to $\delta_L(R)$. Considering Eqs. (6) and (A1), the gradient method can also be expressed as a function of the variance $\langle u_1'^2 \rangle$. Hence, Gaussian error propagation yields:

$$\delta_G(R) = \frac{1}{\langle \epsilon_G \rangle_R} \frac{\partial \langle \epsilon_G \rangle_R}{\partial \langle u_1'^2 \rangle_R} e_{\mathrm{rand}} \langle \langle u_1'^2 \rangle_R \rangle_N = -15\nu \frac{1}{\langle \epsilon_G \rangle_R} \lim_{|r| \to 0} \partial_r^2 f(r) e_{\mathrm{rand}} \langle \langle u_1'^2 \rangle_R \rangle_N = \sqrt{\frac{2L_{11}}{R}}, \tag{25}$$

assuming $R \gg L_{11}$ such that the systematic error is negligible such that $\langle \langle u_1'^2 \rangle_R \rangle_N \approx \langle u_1'^2 \rangle$.

Equations (22), (24), and (25) are expressed as a function of R and L_{11}, which do not reveal the dependency of random errors on the Reynolds number. In addition, this expression relies on large scales that depend on the scale of the energy injection, which makes it difficult to fairly compare the errors between different flows as it is not a universal feature. Therefore, we want to link the averaging window to the Kolmogorov length scale η_K, which only depends on the viscosity and the mean energy dissipation rate. We can rewrite these equations in terms of η_K, R and R_λ as follows:

$$\delta_{I2}(R) = \delta_L(R) = \frac{3}{2} \sqrt{\frac{2L_{11}}{R}} = \frac{3}{2} \sqrt{2 \frac{\eta_K}{R} \frac{L_{11}}{L} \left(\frac{3}{20} R_\lambda^2 \right)^{3/4}} \approx \frac{3}{2} \sqrt{\frac{\eta_K}{R} \left(\frac{3}{20} R_\lambda^2 \right)^{3/4}} \tag{26}$$

$$\delta_G(R) = \sqrt{\frac{2L_{11}}{R}} \approx \sqrt{\frac{\eta_K}{R} \left(\frac{3}{20} R_\lambda^2 \right)^{3/4}} \tag{27}$$

where we have invoked $L_{11}/L \sim 1/2$, which is valid at sufficiently high R_λ and used the relationship $L/\eta_K = \left(\frac{3}{20} R_\lambda^2 \right)^{3/4}$ (Pope, 2000). Following the intuition, the longer the averaging window, the smaller the random error of each method.

Furthermore, Eqs. (26) and (27) provide a mean to choose a suitable averaging window size to achieve a given random error threshold a. Let R_a be the averaging window of size R such that $\delta_i(R) < a$. Then, the required averaging window R_a for ϵ_{I2} and ϵ_L is

$$R_a / \eta_K = \frac{9}{4} \left(\frac{3}{20} R_\lambda^2 \right)^{3/4} \frac{1}{a^2}, \tag{28}$$

where the required averaging window size R_a scales with $R_\lambda^{3/2}$. Similarly, the required averaging window for ϵ_G is

$$R_a / \eta_K = \left(\frac{3}{20} R_\lambda^2 \right)^{3/4} \frac{1}{a^2}. \tag{29}$$
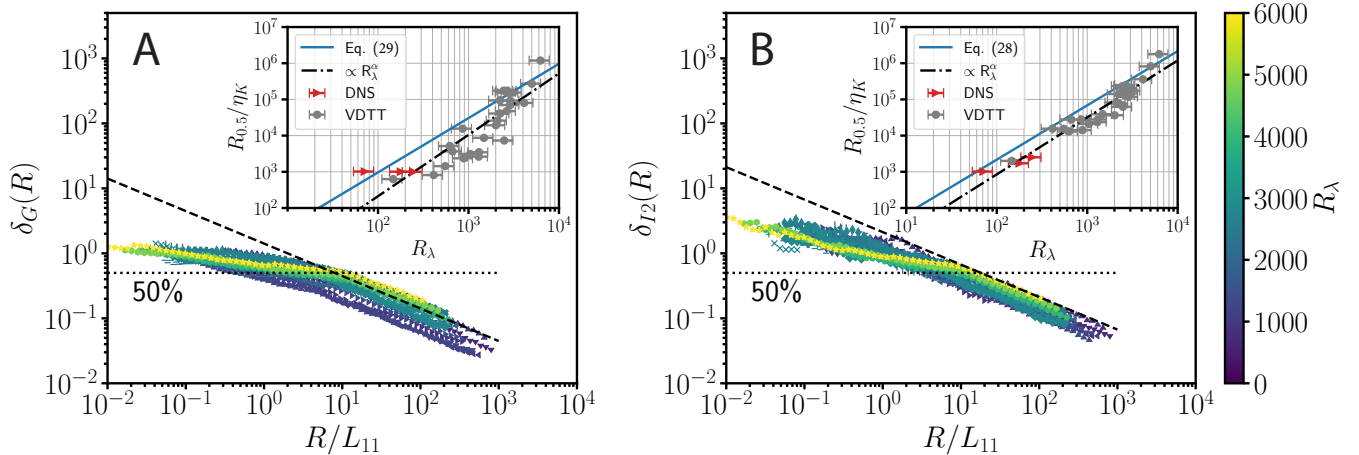
Figure 7. Random errors $\delta_G(R)$ (A) and $\delta_{I2}(R)$ (B) as a function of re-scaled averaging window size R/L_{11} obtained from VDTT data at various R_λ shown by the colorbar. The analytical results for $\delta_G(R)$ (A, Eq. (25)) and $\delta_{I2}(R)$ (B, Eq. (24)) are shown by the dashed black lines. The dotted black line annotated with "50%" in each subplot corresponds to 50% error-threshold. The insets show the sizes of the averaging windows in terms of η_K when $\delta_{G,I2}(R) \leq 0.5$ as a function of Taylor microscale Reynolds number R_λ. The inset plots include data from both DNS (red triangles) and the VDTT (grey circles). DNS data used for the inset plots are from cases 1.3, 2.3 and 3.3 with $I = 10\%$ and $\theta = 0°$. The solid, blue lines show the prediction of the required averaging window according to Eq. (29) (A-inset) and Eq. (28) (B-inset). The black dash-dotted line in inset plots is a fit to the data: $\log R/\eta_K = \frac{3}{4} \log \frac{3}{20} - 2 \log a_{\mathrm{fit}} + \alpha \log R_\lambda$ yielding $\alpha = 1.70 \pm 0.18$ and $a_{\mathrm{fit}} = 1.67 \pm 0.64$ (A-inset); $\log R/\eta_K = \log \frac{9}{4} \frac{3}{20}^{3/4} - 2 \log a_{\mathrm{fit}} + \alpha \log R_\lambda$ yielding $\alpha = 1.57 \pm 0.09$ and $a_{\mathrm{fit}} = 0.95 \pm 0.32$ (B-inset).

For example, for the random errors of ϵ_{I2} and ϵ_L to be less than 10% at $R_\lambda = 1000$, the averaging window should be $R \sim 2 \times 10^6 \eta_K \sim 2 \times 10^4 L_{11}$, while for ϵ_G the required averaging window is $R \sim 8 \times 10^5 \eta_K \sim 10^4 L_{11}$.

Figure 7 shows the empirical random errors $\delta_G(R)$ (Fig. 7A) and $\delta_{I2}(R)$ (Fig. 7B) as a function of the averaging window size for various R_λ based on VDTT data (for ϵ_L see supplementary Fig. A5). To do this, we select an averaging window of size R, where $1000\eta_K < R < \mathcal{O}(10^6 \eta_K)$, from the beginning of each $30\,\mathrm{s}$ time-segment from the VDTT longitudinal velocities are recorded (a total of 47 to 597 time-segments depending on R_λ).

The scaling of $\delta_G(R)$ and $\delta_{I2}(R)$ is well predicted for $R \gtrsim 10 L_{11}$ as expected from Eqs. (25) and (24) and the assumptions we made to derive them. However, for smaller R a statistical convergence of ϵ_G, ϵ_{I2} or ϵ_L against the mean energy dissipation rate cannot be expected, in particular when $R/L_{11} < 1$.

Furthermore, it is evident from Fig. 7 that the random errors do not fully collapse on each other for different Reynolds numbers and at a given R/L_{11}. Moving horizontally on a line of constant random error, e.g., the dashed line of 50% error, the required window size increases with R_λ, as shown in the insets of Figs. 7A and B. Predictions of Eqs. (28) and (29) are also shown in these plots via solid/blue lines.

For both ϵ_G and ϵ_{I2}, the theoretical expectation for R_a tends to overestimate the actual averaging window size at which a random error of 50% is achieved. This overestimation is expected as the theoretical expectation for R_a, Eqs. (28) and (29), are derived assuming that large-scale quantities such as $f(r)$ and L_{11} are fully converged. However, ϵ_G is technically relying on small scales. ϵ_G depends on velocity fluctuation gradients, which are numerically obtained by central differences. Hence, each

25

increment in the velocity record contributes to the average in the gradient method, Eq. (6). In the case of ϵ_{I2}, the number of possible increments reduces for larger separations for a finite averaging window. By definition, the exact computation of L_{11} requires even a fully converged $f(r)$ for all r.

However, VDTT experiments with $R_\lambda > 3000$ underestimate the prediction of Eq. (20) by about a factor of 2. This is particularly clear for ϵ_L shown in Fig. A5. This deviation at high R_λ can be explained, at least in part, by the strong assumptions made for the derivation of the random errors, i.e., the equations (24), (22), and (25). In particular, for experiments with high Re in VDTT, the assumption of Gaussian velocity fluctuations with zero skewness is questionable, as shown in Fig. A6. Lenschow et al. (1994) has already established that the size of the averaging window for a skewed Gaussian process (see Eq. (19) in Lenschow et al., 1994) must be twice as large as for a Gaussian process with vanishing skewness. However, further work is needed to investigate these deviations and improve the theoretical prediction.

3.6   Estimating the transient energy dissipation rate

As it has been shown in previous Figs. 6 and 7, both systematic and random error decrease with the size of the averaging window. For a correct estimate of the magnitude, it is therefore advantageous to choose the averaging window as large as possible, but this has the price that the transient trend smaller than the selected window size cannot be reproduced. In addition, it is also important to know to what extent the estimated trend correlates with the actual trend. Given a certain averaging window size R, here, we empirically evaluate if trends in the coarse-grained time-series are physical or rather statistical. In other words, we ask the question if local estimates of the mean energy dissipation rate follow the ground-truth reference $\langle \epsilon_0(\boldsymbol{x}, t) \rangle_{\mathrm{VP},R}$ or not. Respecting the intermittent nature of turbulence and energy dissipation, the standard deviation of $\langle \epsilon_0(\boldsymbol{x}, t) \rangle_{\mathrm{VP},R}$ is a first proxy for the variability of the trend in $\langle \epsilon_0(\boldsymbol{x}, t) \rangle_{\mathrm{VP},R}$. Hence, detecting the true trend requires that β_i and $\delta_i(R)$ are smaller than the standard deviation of $\langle \epsilon_0(\boldsymbol{x}, t) \rangle_{\mathrm{VP},R}$.

It can be already concluded from Figs. 2, 7, A1 and A5 that ϵ_G is the most promising candidate to capture the true trend. However, to fully answer the above questions, we need to conduct a more in-depth analysis. The upper plot in Fig. 8 shows the re-scaled and coarse-grained dissipation field $\langle \epsilon_0(\boldsymbol{x}, t) \rangle_{\mathrm{VP},R}$ for a sliding window of size $R \approx 5500\eta_K$ and a turbulence intensity $I = 10\%$ obtained from the time series of one virtual probe for case DNS 2.0 ("probe 0"). Consistent with results shown earlier, $\langle \epsilon_G \rangle_R$ follows $\langle \epsilon_0(\boldsymbol{x}, t) \rangle_{\mathrm{VP},R}$ best in comparison with $\langle \epsilon_{I2} \rangle_R$ and $\langle \epsilon_L \rangle_R$. Both $\langle \epsilon_{I2} \rangle_R$ and $\langle \epsilon_L \rangle_R$ are associated with substantial scatter, although $\langle \epsilon_{I2} \rangle_R$ has smaller deviations from the ground-truth overall. Other probe tracks sample different portions of the flow which is why a quantitative conclusion is not possible from one single probe. A more comprehensive evaluation of which method is able to capture the true trend is conducted below.

The lower plot in Fig. 8 shows $\langle \epsilon_{I2} \rangle_R$ together with the random error of ϵ_{I2} as defined by Eq. (24). Despite the strong scatter, the ground-truth reference is nearly always within the errorbar of ϵ_{I2} with some exceptions, e.g. $r/\eta_K < 5000$ or $r/\eta_K \approx 44000$. It can also be seen that $\langle \epsilon_{I2} \rangle_R$ is, if at all, only weakly correlated with the ground-truth reference $\langle \epsilon_0(\boldsymbol{x}, t) \rangle_{\mathrm{VP},R}$ for a window size of $R/\eta_K \approx 5500$. This shows that it is extremely difficult, if at all possible, to track the true trend with low-resolution time records, which prevents the use of the gradient method.
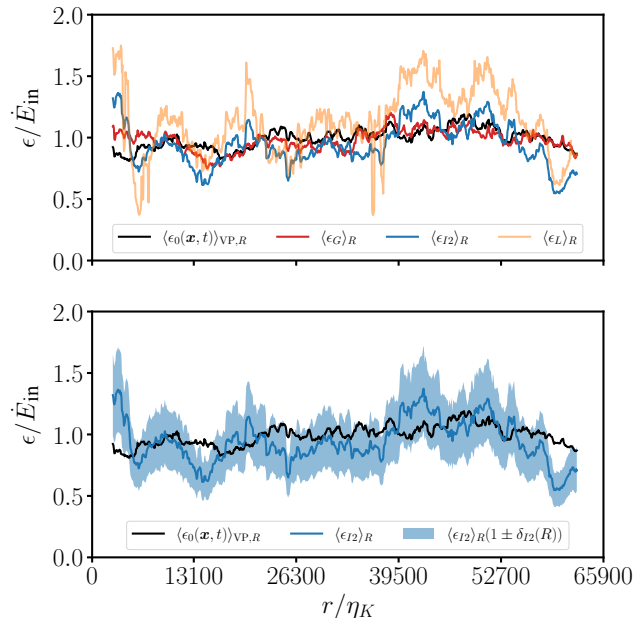
Figure 8. (Upper plot) Proof of concept for estimating the coarse-grained energy dissipation rate $\langle \epsilon_0(\boldsymbol{x},t) \rangle_{\text{VP},R}$ re-scaled by the energy injection rate $\dot{E}_{\text{in}}$ via the one-dimensional surrogates $\langle \epsilon_G \rangle_R$, $\langle \epsilon_{I2} \rangle_R$, and $\langle \epsilon_L \rangle_R$ for $R_\lambda = 142$, $R/\eta_K \approx 5500$, $\theta = 0°$ and a turbulence intensity $I = 10\%$ (DNS 2.0). All estimates are re-scaled by the energy injection rate $\dot{E}_{\text{in}}$, too. We narrowed the fit-range to $20\eta_K \leq r \leq 200\eta_K$ ensuring optimal fit results. (Lower plot) Comparison between $\langle \epsilon_{I2} \rangle_R / \dot{E}_{\text{in}}$ with estimated random error according to Eq. (24) for the averaging window R and $\langle \epsilon_0(\boldsymbol{x},t) \rangle_{\text{VP},R}$.

To assess this correlation more quantitatively, we evaluate Pearson correlation coefficient between the ground-truth reference $\langle \epsilon_0(\boldsymbol{x},t) \rangle_{\text{VP},R}$ and ϵ_G, ϵ_{I2} as well as ϵ_L, respectively, as a function of the re-scaled averaging window size R/η_K for all virtual probes of case DNS 2.0. As an example, Pearson correlation coefficient between $\epsilon_0(\boldsymbol{x},t) \rangle_R$ and ϵ_{I2} is 0.33 in Fig. 8 (upper

600   plot). Figure 9A shows the ensemble averages of Pearson correlation coefficient together with the standard error (shaded area). While $\langle \epsilon_G \rangle_R$ has a pronounced correlation with the ground-truth reference $\langle \epsilon_0(\boldsymbol{x},t) \rangle_{\text{VP},R}$, both $\langle \epsilon_{I2} \rangle_R$ and $\langle \epsilon_L \rangle_R$ are only very weakly correlated with $\langle \epsilon_G \rangle_R$.

The effect of R_λ on Pearson correlation coefficient is shown in Fig. 9B also for the VDTT experiments at various R_λ. Here, we compare ϵ_{I2} and ϵ_L to ϵ_G in the absence of a ground-truth reference. To ensure a negligible systematic error, we chose a

605   fixed averaging window of $R = 30L_{11}$ for each R_λ. Figure 9B shows that the correlation for ϵ_{I2} is always higher than that of ϵ_L except for very low R_λ. There is a non-monotonic behavior in the correlation coefficients in Fig. 9B that seems to be related to the skewness values shown in Fig. A6. Nonetheless, there is a clear increase in correlation coefficients with R_λ. Firstly, the random error of $\delta_{I2}(R)$ ranges from 20% to 40% at $R = 30L_{11}$. Secondly, the kurtosis of the instantaneous energy dissipation field scales with $R_\lambda^{3/2}$ (Pope, 2000) which is why the variability in the instantaneous energy dissipation field increases with R_λ.

610   Hence, at small $R_\lambda^{3/2}$ and $R = 30L_{11}$, $\langle \epsilon_{I2} \rangle_{30L_{11}}$ scatters only randomly around the global mean energy dissipation rate (with a 3% standard deviation of $\langle \epsilon_G \rangle_{30L_{11}}$), which is why the correlation coefficient is low. In contrast, at large R_λ and $R = 30L_{11}$,

the locally averaged mean energy dissipation rate $\langle\epsilon_G\rangle_{30L_{11}}$ fluctuates stronger ($\approx 30\%$ standard deviation of $\langle\epsilon_G\rangle_{30L_{11}}$) where $\delta_{I2}(R)$ is already comparable.
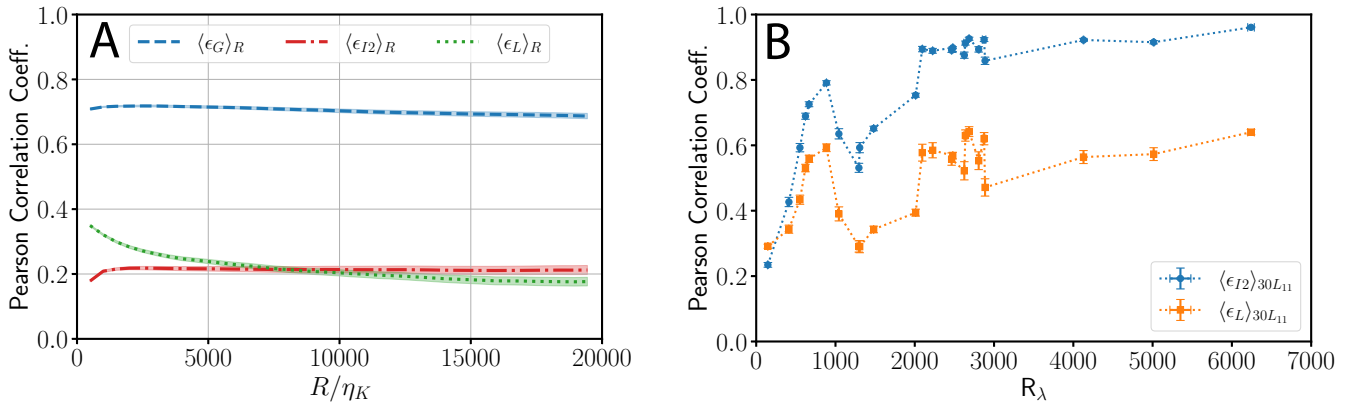
Figure 9. A: Dependence of the Pearson correlation coefficient between $\langle\epsilon_i\rangle_R$ and $\langle\epsilon_0(\boldsymbol{x},t)\rangle_{\mathrm{VP},R}$ as a function of the re-scaled averaging window R/η_K where $i \in \{G,I2,L\}$. Time records of the longitudinal velocity by all virtual probes and $\langle\epsilon_0(\boldsymbol{x},t)\rangle_{\mathrm{VP},R}$ are taken from DNS 2.0 with $\mathrm{R}_\lambda = 142$, turbulence intensity $I = 10\%$ and perfect alignment ($\theta = 0°$). The shaded region is given by the standard error. B: Dependence of the Pearson correlation coefficient between $\langle\epsilon_{I2,L}\rangle_R$ and $\langle\epsilon_G\rangle_R$ as a function R_λ for a fixed re-scaled averaging window $R = 30L_{11}$. The error bars of the ensemble-averaged coefficients are given by the standard error.

4 Practical guidelines

615 Up to this point, we have presented the results largely as is, so that one can interpret them with minimal bias. However, the amount of data given and details may make the use of the results in practice difficult. Therefore, we propose here practical guidelines for measuring the energy dissipation rate from one-dimensional velocity records in atmospheric flows.

The gradient method should be preferred over other methods for conditions where the turbulence intensity is low and the probe could be perfectly aligned in the direction of the mean wind. In particular, the gradient method is more sensitive to
620 turbulence intensity than inertial-range methods due to random sweeping effects. Low values of turbulence intensity and ideal alignment of probes can be best controlled in ground-based measurements. Measurements aboard research aircraft traveling at true speed of $100\,\mathrm{m\,s^{-1}}$ can satisfy these conditions also, but the spatial/temporal resolution required to measure the velocity gradients (see Fig. A8) is challenging to achieve, i.e., a robust probe with a wire length ideally smaller than $1\,\mathrm{mm}$ (or in the same order as η_K) and a true response frequency of $10^5\,\mathrm{Hz}$ is needed. Other airborne platforms, such as helicopters, balloons
625 and kites, would encounter higher turbulence intensities making Taylor's frozen flow assumption more difficult to satisfy. Most importantly, however, they all suffer from probe alignment into the local wind at the scale of the measurement platform.

Other estimates based on inertial sub-range methods (cf. Table 1) are less sensitive to a high turbulence intensity and probe alignment. Regarding the impact of a high turbulence intensity, we find the the most reliable method for most field applications to be the second-order structure function. However the accuracy is least 10% even in most ideal conditions considered here
630 (Table 4). Considering experimental imperfections, the actual deviation is expected to be of the order of 100% (Figs. 3 and 5).

Given atmospheric turbulence with $\eta_K \sim 1\,\mathrm{mm}$ and $L_{11} \sim 100\,\mathrm{m}$, the inertial range of the second-order structure function extends from about $60\eta_K$ (Pope, 2000) to at most the integral scale, if at all. However, for applying the 2nd-order SF (inertial range), at least one to two decades of the inertial range are needed. Assuming that the fitting range is chosen from $0.1\,\mathrm{m}$ to $10\,\mathrm{m}$, a measurement platform with a true air speed of $10\text{-}100\,\mathrm{m\,s^{-1}}$ requires an anemometer with a sampling frequency of 100-1000 Hz in order to provide about two decades of data within the inertial range.

Our analysis further shows that estimating the transient energy dissipation in atmospheric clouds ($L_{11} \sim 100\,\mathrm{m}$, $\mathcal{O}(\mathrm{R}_\lambda) \sim 10^3 - 10^4$) via the 2nd-order structure function (inertial range) with an averaging window of $R = 100\,\mathrm{m}$ is prone to random errors of the order 100% (Fig. 7B). Shorter averaging windows involve even higher random errors. It is therefore recommended to choose the averaging window as large as possible but still smaller than length and time scales on which the atmosphere remains homogeneous and stationary, respectively. This recommendation is not simple to be realized in a atmosphere. for example, measurements in the marine boundary layer with intermittent shallow cumulus clouds stationary conditions needed to be carefully considered Then, two approaches can be recommended. On the one hand, one can choose a *very long* averaging window to average over many individual clouds associated with a small random error but potentially violating the stationary and homogeneity condition. On the other hand, one could investigate the transient mean energy dissipation rate (as a proxy for the local mean energy dissipation rate per cloud) while accepting a large random error.

The large random errors also preclude the possibility of interpreting trends in the measured energy dissipation rate via the second-order structure function when we consider the results shown in Figs. 8 and 9A. Even if we consider the promising correlations shown in Fig. 9B at high Reynolds numbers, interpreting trends and patterns in atmospheric data from one-dimensional time records remains a challenge, especially in an atmosphere with intermittent cloudiness. As an example, in a cloud with a horizontal extent of $1\,\mathrm{km}$, one can obtain 10 non-overlapping data blocks with a window length of $100\,\mathrm{m}$, which corresponds to a random error of about 100% to be combined with a systematic error of the same order of magnitude. With 10 data points combined with such large uncertainties, it would be extremely difficult to interpret the change in dissipation rate in this cloud. Interpretations of trends in the energy dissipation rate would be particularly flawed if the size of the averaging window is $< 10L_{11}$. At best, an average value can be determined for such small clouds, which would still deviate from the global mean by at least 50-100% if (and this is a big if. However, the limitations imposed by the validity of the Taylor hypothesis can be mitigated by using an array of high-resolution anemometers. The array should be oriented so that the anemometers point in the mean local wind direction. The calculation of transverse velocity gradients or second-order structure functions would no longer depend on the applicability of the Taylor hypothesis, since the distances between the sensors are predefined by the design.

5 Summary

We have presented an extensive review on the analysis procedure for estimating the energy dissipation rate from single-point one-dimensional velocity time records along with an overview of the advantages and disadvantages (see Table 1). To conclude, this paper provides means to estimate errors of the global and local mean energy dissipation rates due to experimental imper-

fections and limitations. These error estimated can be used to assess the quality and accuracy of the measurement. Furthermore, error estimates of the global and local mean energy dissipation rates can be used to assess the error of other turbulence and cloud droplet parameters, e.g., various turbulence length scales and the cloud droplet Stokes number, with the help of Gaussian error propagation. A set of practical guidelines for measurement/analysis strategies are provided in the previous section, the following presents a technical summary of the main results.

The main methods considered in this study are the gradient method ϵ_G, the 2nd-order SF (inertial range) method ϵ_{I2}, the spectral method ϵ_S, and the scaling argument ϵ_L. We have provided a systematic assessment of the accuracy of inferring the energy dissipation rate from such one-dimensional velocity time series as a function of turbulence intensity, probe orientation with respect to the longitudinal direction, and the effect of a finite averaging window size. We used DNS data with Reynolds numbers in the range $74 \leq R_\lambda \leq 321$ as well as experimental data from high-resolution one-dimensional wind tunnel measurements with Reynolds numbers in the range $147 \leq R_\lambda \leq 5864$ to evaluate the performance of different methods against robust benchmark values. The results presented in this study help to assess the accuracy of the energy dissipation rate estimates as a function of several parameters, such as finite turbulence intensity, misalignment between sensor and longitudinal flow direction, and finite size of the averaging window. The main results are:

– Each method could reproduce the ground-truth reference $\langle \epsilon(\boldsymbol{x}, t) \rangle$ to within less than 10 % for well converged statistics and at low turbulence intensity. The most accurate method is the gradient method (ϵ_G) and the least accurate method is the one based on the 4/5 law (ϵ_{I3}) (see Fig. 2). The "reference-compared" systematic error tend to be overestimated due to the global choice of the fit-range, e.g., lower systematic errors for ϵ_{I2} can be obtained by choosing a fit-range for each DNS dataset that is in a range where the scaling of the structure function is closest to the expected scaling.

– In the case of finite turbulence intensities, ϵ_G, ϵ_S and ϵ_{I2} systematically overestimate the ground-truth energy dissipation rate. The gradient method (ϵ_G) is most affected by a finite turbulence intensity I whereas ϵ_{I2} is the least affected (see Figs. 3 and 4B). The overestimation can be captured by a random advection model (Fig. 4). Regarding the small-scale estimate ϵ_G, the error formula provided by Lumley (1965) ($\beta_G \propto 5I^2$) captures the effect of random advection.

– Considering the probe orientation, the gradient method (ϵ_G) is most affected by misalignment between the probe orientation and the longitudinal flow direction whereas ϵ_{I2} is the least affected (Fig. 5) (compare Eqs. (19), (17), and (18)).

– We provide scaling arguments $\delta_i(R)$ to estimate the required averaging window size optimized for a desired random error threshold for ϵ_G, Eq. (29), ϵ_{I2}, Eq. (28), and ϵ_L, Eq. (28). With this, we can estimate a coarse-grained energy dissipation rate to within a predicted uncertainty as shown in Fig. 8. Systematic errors β_i are smaller than random errors $\delta_i(R)$ for $R > 2L_{11}$.

– The random error of the gradient method $\delta_G(R)$ converges at least 4-5 times faster than ϵ_{I2} (compare Eqs. (28) and (29)).

– Only ϵ_G reliably estimates the transient energy dissipation rate $\langle \epsilon_0 \rangle_R$ although it is most vulnerable to experimental imperfections/limitations.

Appendix A: Preliminaries on Second-Order Statistics

As discussed in detail below, the mean energy dissipation rate can be related to second-order statistics of the velocity field, either in terms of velocity gradients or in terms of velocity increments. In any case, the two-point velocity covariance tensor turns out to be the central quantity of interest, from which the second-order structure function tensor, the spectral energy tensor and the velocity gradient covariance tensor can be obtained.

In the following, we assume zero-mean SHI turbulence so that two-point quantities depend only on the separation vector $\boldsymbol{r}$, all averages are invariant under rotations of the coordinate system, and the mean squared velocity fluctuation is identical for all velocity components, i.e., $\langle u'^2 \rangle = \langle u_1'^2 \rangle = \langle u_2'^2 \rangle = \langle u_3'^2 \rangle$. We provide an overview of the most relevant definitions, their notation and conventions. This section does not explicitly discuss the effect of the averaging window, but the definitions presented can be applied to windowed inputs with no or straightforward modifications.

Under the given assumptions, the two-point velocity covariance tensor takes the form (e.g. Pope, 2000; Robertson, 1940; Batchelor, 1953)

$$R_{ij}(\boldsymbol{r}) = \langle u_i'(\boldsymbol{x}+\boldsymbol{r},t) u_j'(\boldsymbol{x},t) \rangle = \langle u'^2 \rangle \left(g(r)\delta_{ij} + [f(r)-g(r)]\frac{r_i r_j}{r^2} \right), \tag{A1}$$

Symbol	Definition	Equation	Dimensions
A	large-scale anisotropy parameter	$3\langle u_1'^2\rangle/(2k)$	
C_K	Kolmogorov constant related to $E(\kappa)$	1.5	
C_ϵ	dissipation constant	0.5	
$D_{ij}(\boldsymbol{r})$	second-order velocity structure function tensor	(A2)	L^2T^{-2}
$E(\kappa)$	energy spectrum function	$\iiint_{-\infty}^\infty \frac{1}{2}\Phi_{ii}(\boldsymbol{\kappa})\delta(|\boldsymbol{\kappa}|-\kappa)\mathrm{d}\boldsymbol{\kappa}$	L^3T^{-2}
$E_{11}(\kappa_1)$	one-dimensional energy spectrum	(A7)	L^3T^{-2}
$\dot{E}_\mathrm{in}$	energy injection rate of the DNS		L^2/T^{-3}
$F_{11}(f)$	power spectral density of longitudinal velocity	$\frac{\Delta t}{N}\mathcal{F}(u_1(t))\mathcal{F}^*(u_1(t))$	L^2T^{-1}
$\mathcal{F}(x)$	(discrete) Fourier transform	$\sum_{j=0}^{N-1} x(t_j)\exp(-2\pi it_j/\Delta t)$	
I	turbulence intensity	$\sigma_{u_1'}/U$	
L	length scale characteristic of large eddies, e.g. energy injection scale	$k^{3/2}/\epsilon$	L
L_{11}	longitudinal integral length scale of the turbulent flow	(11)	L
$R_{ij}(\boldsymbol{r})$	velocity (two-point, one-time velocity auto-) covariance tensor	(A1)	L^2T^{-2}
$R_{ijkl}(\boldsymbol{r})$	velocity gradient covariance tensor	(A4)	T^{-2}
Re	Reynolds number	$\frac{UL}{\nu}$	
R_λ	Taylor-scale Reynolds number	$\sqrt{\frac{15\sigma_{u_1}^4}{\nu\langle\epsilon\rangle}}$	
Re_L	turbulence Reynolds number	$\frac{k^{1/2}L}{\nu}$	
S_{ij}	strain rate tensor	$(\frac{\partial u_i(\boldsymbol{x},t)}{\partial x_j}+\frac{\partial u_j(\boldsymbol{x},t)}{\partial x_i})/2$	T^{-1}
T	longitudinal integral time scale of the turbulent flow	$\int_0^\infty f(\tau)\mathrm{d}\tau$	T
$\boldsymbol{U}, U_\tau$	global-mean velocity vector of the flow and the local-mean of the longitudinal velocity component for averaging window of duration τ relative to the virtual probe	(1)	LT^{-1}
a_fit	fit parameter related to Eq. (28)		
f	frequency		T^{-1}
$f(r)$	longitudinal velocity auto-correlation [coefficient] function	$R_{11}(r)/R_{11}(0)$	
$g(r)$	transverse velocity auto-correlation [coefficient] function	$f(r)+r\partial_r f(r)/2$	
k	turbulent kinetic energy	$(u_1'^2+u_2'^2+u_3'^2)/2$	L^2T^{-2}
$\boldsymbol{r}, r$	distance vector (or rather radial coordinate) and its absolute value		L
s_{ij}	[velocity] fluctuation strain rate tensor	$(\frac{\partial u_i'(\boldsymbol{x},t)}{\partial x_j}+\frac{\partial u_j'(\boldsymbol{x},t)}{\partial x_i})/2$	T^{-1}
t	time		T
$\boldsymbol{u}$	(Eulerian) velocity vector of the flow	$u_1\boldsymbol{e}_1+u_2\boldsymbol{e}_2+u_3\boldsymbol{e}_3$	LT^{-1}
$\boldsymbol{u}'$	velocity fluctuation vector of the flow	$\boldsymbol{u}-\boldsymbol{U}$	LT^{-1}
$\langle u_1'^2\rangle$	variance of longitudinal velocity fluctuations	$\int_0^\infty E_{11}(\kappa_1)\mathrm{d}\kappa_1$	L^2T^{-2}
$\boldsymbol{x}$	position vector	$x_1\boldsymbol{e}_1+x_2\boldsymbol{e}_2+x_3\boldsymbol{e}_3$	L
$\Phi_{ij}(\boldsymbol{\kappa})$	energy tensor (velocity spectrum tensor)	(A5)	L^5T^{-2}
α	fit parameter related to Eq. (28)		
δ_{ij}	Kronecker delta		
Δt	time increment	$\min\{t_{j+1}-tj\}$	T
ϵ	energy dissipation rate		L^2T^{-3}
$\epsilon_0(\boldsymbol{x},t)$	instantaneous energy dissipation rate	(3)	L^2T^{-3}
ϵ_R	locally volume averaged energy dissipation rate	(4)	L^2T^{-3}
$\langle\epsilon\rangle$	global-mean energy dissipation rate (rate of dissipation of turbulent kinetic energy)	(5)	L^2T^{-3}
ϵ_{ijk}	Levi-Cevita tensor		
ζ_n	nth-order structure function exponent	$\frac{\mathrm{d}\log D_{L\ldots}(r)}{\mathrm{d}\log r}$	
η_K	Kolmogorov length scale	$(\nu^3/\langle\epsilon\rangle)^{1/4}$	L
θ	angle of incidence between probe orientation and longitudinal flow direction		$°$
$\boldsymbol{\kappa}$	wave vector		L
λ	longitudinal Taylor (micro-)scale	$\sqrt{\frac{30\nu u_1'^2}{\langle\epsilon\rangle}}$	L
ν	kinematic viscosity		L^2T^{-1}
σ_x	standard deviation of quantity x		
$\sigma_{u_1'}$	root mean square of longitudinal velocity fluctuations		LT^{-1}
ω	angular frequency	$2\pi f$	T
$\langle\ldots\rangle_N$	ensemble average over trajectories of N virtual probes or N realizations		
$\langle\ldots\rangle_R$	volume average [line average for 1D signal]		
$\langle\ldots\rangle_\mathrm{VP}$	average over trajectory of a virtual probe		

Table A1. Nomenclature for the turbulent flow. If our naming convention differs from the terminology in (Pope, 2000), we add the convention of Pope in parentheses. Equations are either directly given or referenced from definitions below.

Symbol	Definition
1, 2, 3	indices of vectors and tensors
C	cutoff
D	dissipation range
G	gradient
$I2$	inertial range of second-order structure function
$I3$	inertial range of third-order structure function
L	longitudinal
N	number of virtual probes used in the DNS simulations, number of realizations
$N\ldots$	transverse (e.g. NN for transverse second-order structure function)
R	averaging window size in space
S	inertial range of the power spectral density
p	probe
ref	(ground-truth) reference
VP	virtual probe
τ	averaging window size in time

Table A2. Nomenclature for the subscripts.

DNS	$\langle\beta_G\rangle_N$	$\langle\beta_{I3}\rangle_N$	$\langle\beta_{I2}\rangle_N$	$\langle\beta_S\rangle_N$	$\langle\beta_L\rangle_N$
1.1	-0.003 ± 0.001	0.132 ± 0.005	-0.047 ± 0.002	0.011 ± 0.002	-0.044 ± 0.003
2.1	-0.002 ± 0.006	0.506 ± 0.038	-0.011 ± 0.014	0.074 ± 0.010	0.313 ± 0.017
3.1	-0.005 ± 0.006	0.492 ± 0.039	0.088 ± 0.013	0.041 ± 0.010	0.400 ± 0.020

Table A3. The systematic error of each method β_i relative to the global mean energy dissipation rate, Eq. (12), of each DNS where $i \in \{G, I3, I2, S, L\}$. The error is given by the standard error, which is defined as the standard deviation divided by the square root of the number of samples. In both DNS 2.1 and 3.1, ϵ_{I2} and ϵ_{I3} were obtained by fitting Eq. (7) for $n = 2$ and $n = 3$, respectively, in the range $r \in [20\eta_K, 500\eta_K]$. This fit-range is also used for calculating ϵ_S and it was converted into frequency domain by $f = U/r$, where U is the mean velocity. In the case of DNS 1.1, the maximum of Eq. (7) was used to infer ϵ_{I2} due to the absence of a pronounced inertial range. We used the maximum available window size R in all cases, fixed turbulence intensity $I = 1\%$ and considered perfect alignment, i.e., $\theta = 0°$.

where $f(r) = R_{11}(r)/R_{11}(0)$ and $g(r) = f(r) + r\partial_r f(r)/2$ are the longitudinal and transverse autocorrelation functions, respectively, with $f(0) = g(0) = 1$. Notably, if one chooses $\boldsymbol{r} = r\boldsymbol{e}_1$, $R_{11}(r) = \langle u'^2\rangle f(r)$, $R_{22}(r) = R_{33}(r) = \langle u'^2\rangle g(r)$, and all other components vanish (e.g., Pope, 2000). As a remarkable consequence, $R_{ij}(\boldsymbol{r})$ is uniquely defined by $f(r)$ in isotropic turbulence. As mentioned below, the integral length scale as well as the Taylor microscale are determined by $f(r)$ (Pope, 2000).

Analogously, a covariance tensor can be defined for velocity increments, i.e. the second-order velocity structure function tensor (Pope, 2000; Davidson, 2015)

$$D_{ij}(\boldsymbol{r}) = \langle [u'_i(\boldsymbol{x}+\boldsymbol{r},t) - u'_i(\boldsymbol{x},t)][u'_j(\boldsymbol{x}+\boldsymbol{r},t) - u'_j(\boldsymbol{x},t)]\rangle = D_{NN}(r)\delta_{ij} + [D_{LL}(r) - D_{NN}(r)]\frac{r_i r_j}{r^2}. \tag{A2}$$

The longitudinal second-order structure function $D_{11}(r)$ is related to $f(r)$ by (e.g., Pope, 2000; Davidson, 2015)

$$D_{11}(\boldsymbol{r} = r\boldsymbol{e}_1) = D_{LL}(r) = \langle (u_1'(\boldsymbol{x} + r\boldsymbol{e}_1, t) - u_1'(\boldsymbol{x}, t))^2 \rangle = 2\langle u'^2 \rangle (1 - f(r)). \tag{A3}$$

As explained below, measuring the longitudinal second-order structure function $D_{LL}(r)$, the mean energy dissipation rate can be inferred from the inertial-range scaling of the longitudinal structure function (cf. Eq. (7)).

Furthermore, the velocity gradient covariance tensor can also be defined in terms of the velocity covariance tensor

$$R_{ijkl}(\boldsymbol{r}) = \left\langle \frac{\partial u_i'(\boldsymbol{x}, t)}{\partial x_k} \frac{\partial u_j'(\boldsymbol{x}, t)}{\partial x_l} \right\rangle = -\lim_{r \to 0} \partial_{r_k} \partial_{r_l} R_{ij}(\boldsymbol{r}). \tag{A4}$$

Since the local and instantaneous energy dissipation rate (cf. Eq. (3)) is defined in terms of the strain rate tensor $S_{ik} = (\partial u_i'(\boldsymbol{x}, t)/\partial x_k + \partial u_k'(\boldsymbol{x}, t)/\partial x_i)/2$, the mean energy dissipation rate can be directly related to contractions of the velocity gradient covariance tensor. Note that in a turbulent flow with zero-mean velocity, the strain rate tensor S_{ik} equals the fluctuation strain rate tensor s_{ik}.

The two-point velocity covariance tensor can be expressed in Fourier space through the spectral energy tensor (Pope, 2000)

$$\Phi_{ij}(\boldsymbol{\kappa}) = \frac{1}{(2\pi)^3} \iiint\limits_{-\infty}^{+\infty} R_{ij}(\boldsymbol{r}) e^{-i\boldsymbol{\kappa} \cdot \boldsymbol{r}} \mathrm{d}\boldsymbol{r}, \tag{A5}$$

where $\boldsymbol{\kappa}$ is the wave vector. For SHI turbulence, $\Phi_{ij}(\boldsymbol{\kappa})$ takes the form

$$\Phi_{ij}(\boldsymbol{\kappa}) = \frac{E(\kappa)}{4\pi\kappa^2} \left(\delta_{ij} - \frac{\kappa_i \kappa_j}{\kappa^2} \right) \tag{A6}$$

where $E(\kappa)$ is the energy spectrum function.

Since access to the full energy spectrum function is not always available, one-dimensional spectra are of interest, too. The mean energy dissipation rate can be estimated from the inertial range scaling of the longitudinal one-dimensional spectrum (as shown in Eq. (9)), which can be calculated by both the energy spectrum function and the velocity covariance tensor (Pope, 2000)

$$E_{11}(\kappa_1) = \int\limits_{\kappa_1}^{\infty} \frac{E(\kappa)}{\kappa} \left(1 - \frac{\kappa_1^2}{\kappa^2} \right) \mathrm{d}\kappa = \frac{1}{\pi} \int\limits_{-\infty}^{\infty} R_{11}(\boldsymbol{e}_1 r_1) e^{-i\kappa_1 r_1} \mathrm{d}r_1, \tag{A7}$$

with the wavenumber κ_1 corresponding to the $\boldsymbol{e}_1$-direction and $R_{11}(0) = \langle u'^2 \rangle = \int_0^\infty E_{11}(\kappa_1) \mathrm{d}\kappa_1$.

This concludes the second-order statistics in terms of the velocity that we consider in the following to determine the mean energy dissipation rate.

Appendix B: Impact of random sweeping effects on gradient method

In the following, we illustrate how one obtains an expression for the impact of random sweeping effects on the dissipation rate estimate in terms of the turbulence intensity using the gradient method $\epsilon_G = \langle\epsilon\rangle[1+5I^2]$ Lumley (1965); Wyngaard and Clifford (1977). We consider a model wavenumber-frequency spectrum (Wilczek and Narita, 2012; Wilczek et al., 2014), which is based on the same modeling assumptions used in Wyngaard and Clifford (1977). It enables us to conduct a systematic assessment of the interplay between Taylor's hypothesis and the random sweeping effects. The model wavenumber-frequency spectrum tensor $\Phi_{ij}(\boldsymbol{\kappa},\omega)$ can be derived from an elementary linear random advection model (Kraichnan, 1964; Wilczek and Narita, 2012; Wilczek et al., 2014), which in case of SHI turbulence can be expressed in terms of the energy spectrum tensor $\Phi_{ij}(\boldsymbol{\kappa})$:

$$\Phi_{ij}(\boldsymbol{\kappa},\omega) = \frac{\Phi_{ij}(\boldsymbol{\kappa})}{\sqrt{2\pi\kappa^2 I^2 U^2}} \exp\left(-\frac{(\omega/U - \kappa_1)^2}{2\kappa^2 I^2}\right). \tag{B1}$$

Within the model, the wavenumber-frequency spectrum $\Phi_{ij}(\boldsymbol{\kappa},\omega)$ consists of the energy spectrum tensor in wavenumber space $\Phi_{ij}(\boldsymbol{\kappa})$ multiplied by a Gaussian frequency distribution. $\Phi_{ij}(\boldsymbol{\kappa})$ has a mean value determined by $\omega = \kappa_1 U$, i.e., Taylor's hypothesis expressed in Fourier space, and a variance proportional to the turbulence intensity. When the turbulence intensity tends to zero at fixed mean velocity, the frequency distribution tends to a delta function, re-establishing the one-to-one correspondence between the frequency and the wavenumber in the direction of the mean flow. To establish the connection to the different methods using longitudinal components and Taylor's hypothesis, we consider the $i = j = 1$ component of Eq. (B1). One obtains the estimate for the longitudinal wavenumber spectrum based on Taylor's hypothesis, which includes the effect of random sweeping, by first integrating over the wavevector space. This leads to the frequency spectrum $\tilde{F}_{11}(\omega)$, which corresponds to the one obtained from temporal single-point measurements of the longitudinal velocity component. Then, one applies Taylor's hypothesis, corresponding to the substitution $\omega = \kappa_1 U$ which leads to

$$E_{11}(\kappa_1)d\kappa_1 \overset{\omega=\kappa_1 U}{=} \frac{1}{U}\tilde{F}_{11}(\omega)d\omega = \frac{2}{U}\left[\int \Phi_{11}(\boldsymbol{\kappa}',\omega)d\boldsymbol{\kappa}'\right]d\omega. \tag{B2}$$

Finally, this enables us to evaluate the influence of random sweeping on the gradient method since it is closely related to the wavenumber spectrum. Expressed in wavenumber space, the relation, Eq. (6), takes the following form, where we insert Eqs. (B1)-(B2) and solve the corresponding Gaussian integral over ω in the second step:

$$\epsilon_G = 15\nu \int \kappa_1^2 E_{11}(\kappa_1)d\kappa_1 = \langle\epsilon\rangle[1+5I^2]. \tag{B3}$$

Hence, we recover, as expected, the result by Lumley (1965) and Wyngaard and Clifford (1977).

To numerically assess how random sweeping smears out the spectrum at finite turbulence intensities (see Fig. 4), we assumed a model wavenumber spectrum, (Pope, 2000, Eq. 6.246 ff.):

$$E(\kappa) = C_K \langle \epsilon \rangle^{2/3} \kappa^{-5/3} \left(\frac{\kappa L}{[(\kappa L)^2 + c_L]^{1/2}} \right)^{5/3 + p_0} \exp(-\beta \kappa \eta_K), \tag{B4}$$

where L is the energy injection scale and $c_L = 6.78$, $p_0 = 2$ and $\beta = 2.094$ are positive constants. Based on this model wavenumber spectrum we first obtain $E_{11}(\kappa)$ through Eq. (A7). One can then evaluate Eq. (B2) resulting in the spectrum being smeared out by random sweeping.

Appendix C: Effect of Probe Misalignment

Here, we derive estimates for the systematic error due to misalignment between the (virtual) anemometer and the global mean wind direction $\frac{U}{|U|}$. This misalignment is captured by an angle θ, which is assumed to be constant in time and space. In general, the rotation matrix around an arbitrary rotation axis $\hat{n}$ with $n_i n_i = 1$ is given by $\mathcal{R}_{ij}^{\hat{n}}(\theta) = (1 - \cos \theta) n_i n_j + \cos \theta \delta_{ij} + \sin \theta \epsilon_{ijk} n_k$ (e.g., Cole, 2015; Hanson, 2011), where ϵ_{ijk} is the Levi-Cevita tensor and δ_{ij} the Kronecker delta. At first, we consider the covariance tensor $R_{ij}(\boldsymbol{r}')$ since the integral length scale, the second-order structure function tensor as well as the velocity gradient covariance tensor depend on $R_{ij}(\boldsymbol{r}')$ (Eqs. (A1), (A2) and (A4), respectively). In the sensor frame of reference, the covariance tensor is given by

$$R_{ij}(\boldsymbol{r}') = \langle u'^2 \rangle \left(g(r') \delta_{ij} + [f(r') - g(r')] \frac{r_i' r_j'}{r'^2} \right), \tag{C1}$$

where $r_i' = \mathcal{R}_{ij}^{\hat{n}}(\theta) r_j$ and $r' = r$. As only the longitudinal component in the sensor frame of reference is measured, Eq. (C1) reads for $i = j = 1$ and $\boldsymbol{r} = r \boldsymbol{e}_1$

$$R_{11}(\boldsymbol{r}') = \langle u'^2 \rangle \left(g(r) + [f(r) - g(r)] \frac{\mathcal{R}_{1l}^{\hat{n}}(\theta) r_l \mathcal{R}_{1k}^{\hat{n}}(\theta) r_k}{r^2} \right) \tag{C2}$$

$$= \langle u'^2 \rangle \left(g(r) + [f(r) - g(r)] \left(\cos^2 \theta + n_1^4 (1 - \cos \theta)^2 + 2 n_1^2 (1 - \cos \theta) \cos \theta \right) \right). \tag{C3}$$

For further simplification, we assume without loss of generality that the mean wind changes direction only in the horizontal plane. With this we can set $\hat{n} = \boldsymbol{e}_3$, which yields for $\boldsymbol{r}' = r' \boldsymbol{e}_1'$

$$R_{11}(r' \boldsymbol{e}_1') / \langle u'^2 \rangle = f(r') = \langle u'^2 \rangle \left(g(r) + [f(r) - g(r)] \cos^2 \theta \right), \tag{C4}$$

which we interpret as the measured autocorrelation function. Then, the measured longitudinal integral length scale, Eq. (11), amounts to

$$L'_{11}(\theta) = \int_0^\infty dr' f(r') = \int_0^\infty dr \cos\theta (\cos^2\theta f(r) + (1 - \cos^2\theta)g(r)) = \frac{1}{2}L_{11}\cos\theta \left(1 + \cos^2\theta\right), \tag{C5}$$

where the integration of $f(r)$ and $g(r)$ is carried out in the last step, see Eq. (11), while considering the fact that $L_{22} = L_{11}/2$ for isotropic turbulence (Pope, 2000).

An analogous argument also holds for the second-order structure function tensor, Eq. (A2):

$$D_{11}(r') = D_{NN}(r) + [D_{LL}(r) - D_{NN}(r)]\cos^2\theta = D_{LL}(r)\left(\frac{4 - \cos^2\theta}{3}\right), \tag{C6}$$

where the transverse second-order structure function $D_{NN}(r) = D_{22}(r) = D_{33}(r)$ is expressed as $D_{NN}(r) = 4D_{LL}(r)/3 = 4C_2(r\epsilon)^{2/3}/3$ in SHI turbulence (Pope, 2000).

The misalignment error for the gradient method can be estimated analytically starting from the longitudinal component of the velocity gradient covariance tensor R_{1111} — it can be also expressed in terms of the velocity covariance tensor Eq. (A4). Following similar arguments as above and starting from Eq. (A4), assuming $\boldsymbol{r} = r\boldsymbol{e}_1$ and applying the rotation about an axis $\hat{\boldsymbol{n}}$ with $n_i n_i = 1$, we obtain
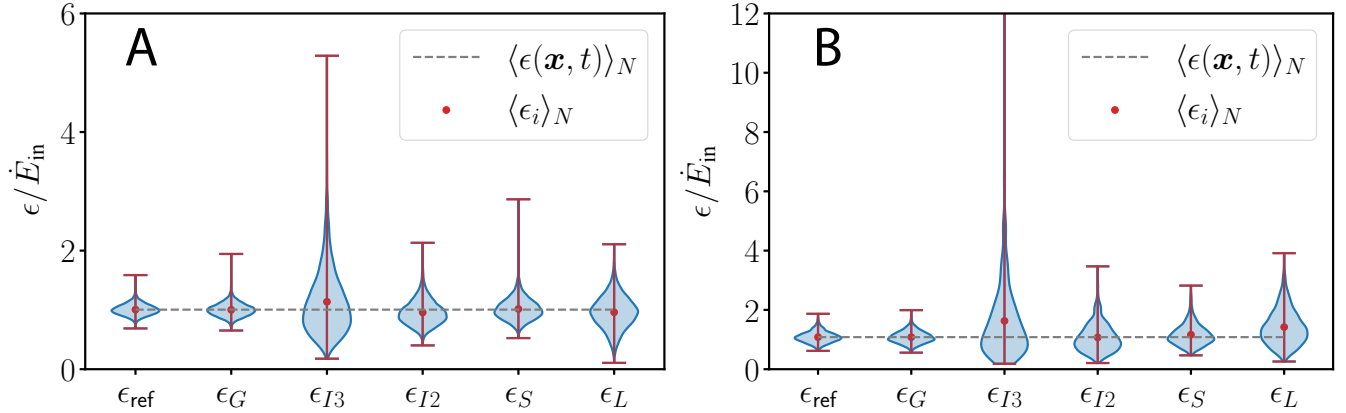
$$R_{1111}(0) = -\lim_{r'\to 0}\partial_{r'}\partial_{r'}R_{11}(r'\boldsymbol{e}'_1) = -\frac{u'^2}{\cos^2\theta}\lim_{r\to 0}\partial_r^2\left[g(r) + [f(r) - g(r)]\frac{r^2\cos^2\theta}{r^2}\right], \tag{C7}$$

where $\partial_{r'} = \partial_r/\cos\theta$ due to the rotation. Using $\partial_r^2 g(r) = 2\partial_r^2 f(r) + \frac{r}{2}\partial_r^3 f(r)$ (Pope, 2000), the velocity gradient covariance tensor reduces to

$$R_{1111}(0) = -\frac{u'^2}{\cos^2\theta}\lim_{r\to 0}\left[(2 - \cos^2\theta)\partial_r^2 f(r) + (1 - \cos^2\theta)\frac{r}{2}\partial_r^3 f(r)\right] \tag{C8}$$

$$= \left\langle\left(\frac{\partial u}{\partial x_1}\right)^2\right\rangle\frac{2 - \cos^2\theta}{\cos^2\theta}, \tag{C9}$$

where $-u'^2\lim_{r\to 0}\partial_r^2 f(r) = \langle(\partial u/\partial x_1)^2\rangle$ (Pope, 2000) is used for the last step.

Figure A1. Validation of estimating the energy dissipation rate from $\epsilon_G, \epsilon_{I2}, \epsilon_{I3}, \epsilon_S,$ and ϵ_L. All estimates are re-scaled by the energy injection rate $\dot{E}_{in}$. The data is taken from DNS 1.1 (A) and 2.1 (B), turbulence intensity $I = 1\%$. The ensemble mean of each method $\langle \epsilon_i \rangle_N$ is denoted by red dots where the whiskers extend from the minimal to maximal estimate of ϵ_i where $i \in \{G, I3, I2, S, L\}$. As the inertial range of DNS 1.1 ($I = 1\%$, $\theta = 0°$ and maximal available averaging window) is not well pronounced due to the low $R_\lambda \sim 74$, we used the maximum of Eq. (7) in order to retrieve $\epsilon_{I2,3}$. The dashed line represents the global mean energy dissipation rate of DNS 1.1 and 2.1 ($R_\lambda = 219$, $I = 1\%$, $\theta = 0°$ and maximal available averaging window), respectively, which is approximated by the ensemble average of the true mean energy dissipation rate along the trajectory of each virtual probe. ϵ_{ref} is the reference distribution of ground-truth global mean energy dissipation field originating from the dissipation field along the trajectory of each virtual probe.
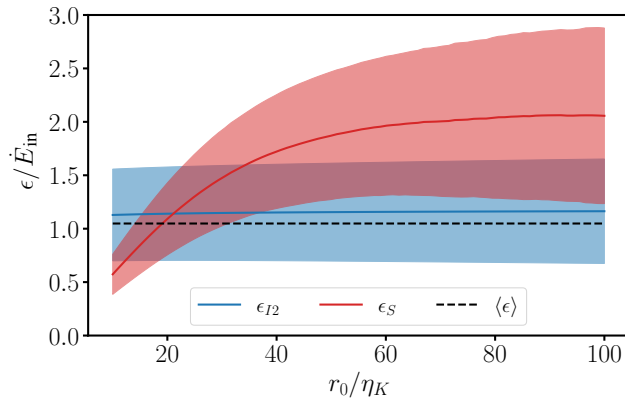

Figure A2. Estimates of the mean energy dissipation rate as a function of the fit-range for ϵ_{I2} and ϵ_S for DNS 3.1 (1000 probes, $R_\lambda = 302$, $I = 1\%$, $\theta = 0°$ and maximal available averaging window) re-scaled by the energy injection rate $\dot{E}_{in}$. The solid line represents the ensemble average whereas the shaded region is given by the standard deviation. $r_0 \in [10\eta_K, 100\eta_K]$ is the lower boundary of the fit-range for ϵ_{I2} where the upper boundary is fixed at $r_1 = 500\eta_K$. For ϵ_S, the fit-range is given by $f \in [U/r_1, U/r_0]$. The dashed line denotes the global mean energy dissipation rate.
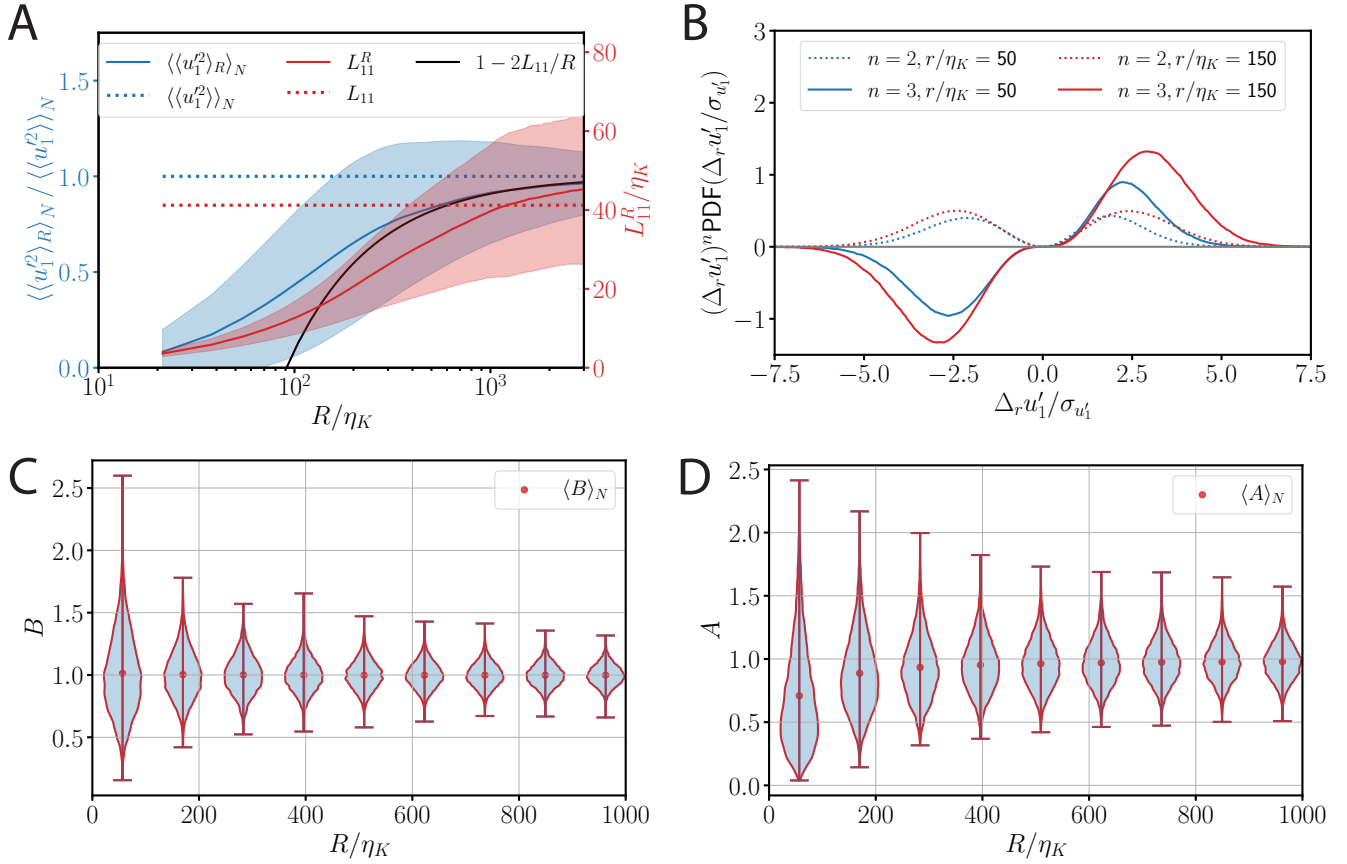
Figure A3. Convergence of higher-order statistical quantities and longitudinal integral length scale as well as small and large-scale anisotropy obtained from all virtual probes of DNS 1.1 ($R_\lambda = 74$, $I = 1\%$, $\theta = 0°$). (A) The variance of the longitudinal velocity fluctuations $\langle u_1'^2 \rangle$ and the longitudinal integral length scale L_{11}^R as a function of averaging window size R normalized by the Kolmogorov length scale η_K. $\langle u_1'^2 \rangle$ re-scaled by the ensemble-averaged variance of the longitudinal velocity fluctuations. For large R, $\langle\langle u_1'^2 \rangle_R \rangle_N$ converges to $\langle u_1'^2 \rangle \approx \langle\langle u_1'^2 \rangle\rangle_N$ (blue-dotted line) and the systematic error of the variance (solid-black line), Eq. (20), decays to 0. L_{11}^R is the longitudinal integral length scale obtained from averaging windows of size R. For large R, L_{11}^R should converge to L_{11} (red-dotted line) which is not fully achieved in this range of R. (B) Premultiplied PDFs of second and third-order velocity increments over distances $r = 50\eta_K$ and $r = 150\eta_K$. The tails of the pre-multiplied PDFs have decayed to zero for large (and re-scaled) increments $\Delta_r u_1'/\sigma_{u_1'}$ so that they can globally considered to be converged. (C) Small-scale anisotropy based on the ratio of longitudinal gradients to the instantaneous energy dissipation $B = \epsilon_G/\langle\epsilon_0(\boldsymbol{x}, t)\rangle$. In isotropic turbulence, $B = 1$ on average. (D) Large-scale anistropy parameter $A = 3\langle u_1'^2 \rangle/(2k)$ as a function of averaging window R where k is the turbulent kinetic energy and $\langle u_1'^2 \rangle$ the variance of the longitudinal velocity fluctuations. In isotropic turbulence, $A = 1$ on average.
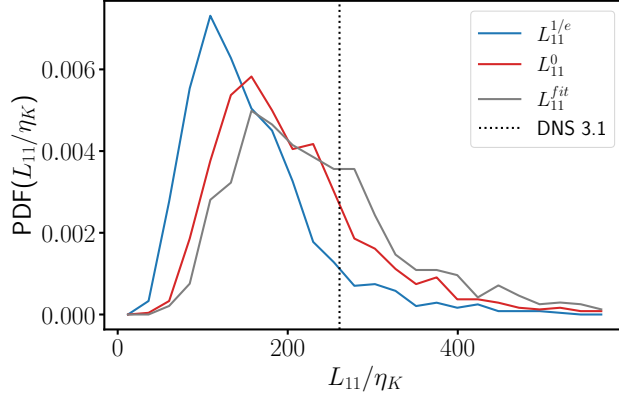
Figure A4. Different estimates of the integral length from DNS 3.1 with $R_\lambda = 302$, $I = 1\%$, $\theta = 0°$ and maximal available averaging window. L_{11}^0 is inferred from integrating $f(r)$ to its first zero whereas $L_{11}^{1/e}$ refers to the integration of $f(r) > 1/e$. L_{11}^{fit} extends $f(r)$ with an exponential tail where the integration is performed up to infinity. The black dotted line is the reference from DNS 3.1 obtained by Eq. (11). All estimates are re-scaled by η_K.
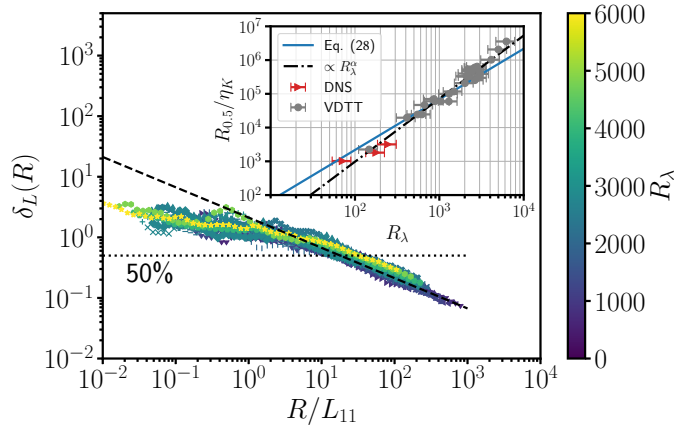

Figure A5. Convergence of energy dissipation rate estimates for ϵ_L. The empirical random error $\delta_L(R)$ is plotted as a function of re-scaled averaging window size R/L_{11} from VDTT experiments at various R_λ. The analytical result for the random error (Eq. (22)) is shown by the dashed black line. (Inset) The insets show the length of the averaging window in terms of η_K where $\hat\delta_L^R$ is less than 50% as a function of Taylor microscale Reynolds number R_λ. The inset plot shows data from DNS 1.3, 2.3 and 3.3 (red triangles) and the VDTT (grey circle). The three red dots mark the experiments with the highest R_λ where the isotropy of the grid forcing in the VDTT is not guaranteed anymore. The solid, blue line shows Eq. (28) resolved for $R_{0.5}/\eta_K$. The double logarithmic fit ($\log R/\eta_K = \frac{3}{4}\log\frac{9}{4}\frac{3}{20} - 2\log a_{\text{fit}} + \alpha\log R_\lambda$) is performed for the scaling argument resulting in $\alpha = 1.87 \pm 0.06$ and $a_{\text{fit}} = 1.75 \pm 0.22$ (black dash-dotted line) .
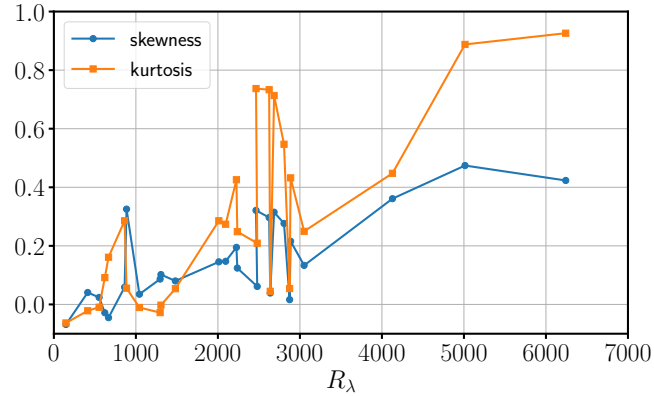
Figure A6. Skewness and kurtosis of all VDTT experiments as a function of R_λ. The skewness vanishes for normally distributed velocity time records. Similarly, the kurtosis equals zero for normally distributed velocity time records, according to Fisher's convention, which is a measure for the excess kurtosis.
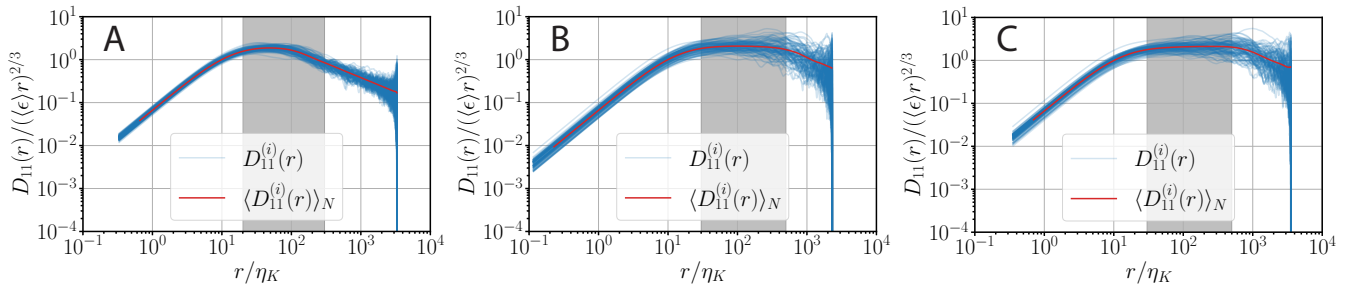
Figure A7. Compensated longitudinal second-order structure functions for DNS 1.1 (A), DNS 2.1 (B), and DNS 3.1 (C). The gray shaded region represents the fit-range (Eq. (7)) for each DNS. The individual longitudinal second-order structure functions are calculated from the velocity time records along the e_1-direction of each virtual probe (blue lines). The ensemble-averaged longitudinal second-order structure functions are shown in red.
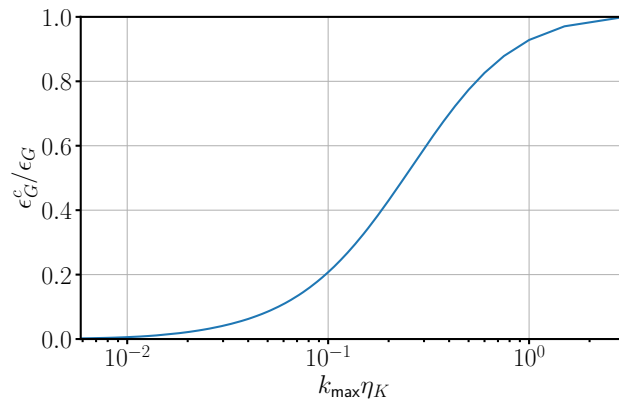
Figure A8. Resolution effect on ϵ_G. ϵ_G^c refers to the coarse-grained velocity time record. Coarse-graining is realized by taking only every nth value of the fully resolved velocity time record where $n \in [1, 512]$, thereby controlling the resolution $k_{\max}\eta_K$. Velocity data are taken from DNS 2.0 ($R_\lambda = 142$, $R \approx 32000\eta_K$, $I = 10\%$, $\theta = 0°$).

References

820   Akinlabi, E. O., Wacławczyk, M., Mellado, J. P., and Malinowski, S. P.: Estimating turbulence kinetic energy dissipation rates in the nu-
       merically simulated stratocumulus cloud-top mixing layer: Evaluation of different methods, Journal of the Atmospheric Sciences, 76,
       1471–1488, 2019.

       Almalkie, S. and de Bruyn Kops, S. M.: Energy dissipation rate surrogates in incompressible Navier–Stokes turbulence, Journal of Fluid
       Mechanics, 697, 204–236, 2012.

825   Antonia, R.: On estimating mean and instantaneous turbulent energy dissipation rates with hot wires, Experimental Thermal and Fluid
       Science, 27, 151–157, 2003.

       Bailey, S. C., Kunkel, G. J., Hultmark, M., Vallikivi, M., Hill, J. P., Meyer, K. A., Tsay, C., Arnold, C. B., and Smits, A. J.: Turbulence
       measurements using a nanoscale thermal anemometry probe, Journal of Fluid Mechanics, 663, 160–179, 2010.

       Batchelor, G. K.: The theory of homogeneous turbulence, Cambridge university press, 1953.

830   Benzi, R., Ciliberto, S., Baudet, C., Chavarria, G. R., and Tripiccione, R.: Extended self-similarity in the dissipation range of fully developed
       turbulence, EPL (Europhysics Letters), 24, 275, 1993a.

       Benzi, R., Ciliberto, S., Tripiccione, R., Baudet, C., Massaioli, F., and Succi, S.: Extended self-similarity in turbulent flows, Physical Review
       E, 48, R29, 1993b.

       Bewley, G. P., Chang, K., and Bodenschatz, E.: On integral length scales in anisotropic turbulence, Physics of Fluids, 24, 061 702, 2012.

835   Bodenschatz, E., Bewley, G. P., Nobach, H., Sinhuber, M., and Xu, H.: Variable density turbulence tunnel facility, Review of Scientific
       Instruments, 85, 093 908, 2014.

       Buaria, D., Pumir, A., Bodenschatz, E., and Yeung, P.-K.: Extreme velocity gradients in turbulent flows, New Journal of Physics, 21, 043 004,
       2019.

       Burattini, P., Lavoie, P., and Antonia, R. A.: On the normalized turbulent energy dissipation rate, Physics of Fluids, 17, 098 103, 2005.

840   Chamecki, M. and Dias, N.: The local isotropy hypothesis and the turbulent kinetic energy dissipation rate in the atmospheric surface layer,
       Quarterly Journal of the Royal Meteorological Society, 130, 2733–2752, 2004.

       Champagne, F.: The fine-scale structure of the turbulent velocity field, Journal of Fluid Mechanics, 86, 67–108, 1978.

       Cole, I. R.: Modelling CPV., Ph.D. thesis, Loughborough University, 2015.

       Davidson, P. A.: Turbulence: an introduction for scientists and engineers, Oxford university press, 2015.

845   Deshpande, S. S., Sathe, M. J., and Joshi, J. B.: Evaluation of local turbulent energy dissipation rate using PIV in jet loop reactor, Industrial
       & Engineering Chemistry Research, 48, 5046–5057, 2009.

       Devenish, B., Bartello, P., Brenguier, J.-L., Collins, L., Grabowski, W. W., IJzermans, R., Malinowski, S. P., Reeks, M., Vassilicos, J., Wang,
       L.-P., et al.: Droplet growth in warm turbulent clouds, Quarterly Journal of the Royal Meteorological Society, 138, 1401–1429, 2012.

       Dodson, D. S. and Small Griswold, J. D.: Turbulent and boundary layer characteristics during VOCALS-REx, Atmospheric Chemistry and
850   Physics, 21, 1937–1961, 2021.

       Donzis, D., Yeung, P., and Sreenivasan, K.: Dissipation and enstrophy in isotropic turbulence: resolution effects and scaling in direct numer-
       ical simulations, Physics of Fluids, 20, 045 108, 2008.

       Elsner, J. and Elsner, W.: On the measurement of turbulence energy dissipation, Measurement Science and Technology, 7, 1334, 1996.

       Fairall, C. and Larsen, S. E.: Inertial-dissipation methods and turbulent fluxes at the air-ocean interface, Boundary-Layer Meteorology, 34,
855   287–301, 1986.

Fairall, C., Markson, R., Schacher, G., and Davidson, K.: An aircraft study of turbulence dissipation rate and temperature structure function in the unstable marine atmospheric boundary layer, Boundary-Layer Meteorology, 19, 453–469, 1980.

Fodor, K. and Mellado, J. P.: New Insights into Wind Shear Effects on Entrainment in Convective Boundary Layers Using Conditional Analysis, Journal of the Atmospheric Sciences, pp. 1–57, 2020.

860 Frehlich, R., Meillier, Y., Jensen, M. L., and Balsley, B.: Turbulence measurements with the CIRES tethered lifting system during CASES-99: Calibration and spectral analysis of temperature and velocity, Journal of the Atmospheric Sciences, 60, 2487–2495, 2003.

Frehlich, R., Meillier, Y., Jensen, M. L., and Balsley, B.: A statistical description of small-scale turbulence in the low-level nocturnal jet, Journal of the atmospheric sciences, 61, 1079–1085, 2004.

Freire, L. S., Dias, N. L., and Chamecki, M.: Effects of path averaging in a sonic anemometer on the estimation of turbulence-kinetic-energy

865 dissipation rates, Boundary-Layer Meteorology, 173, 99–113, 2019.

Garratt, J. R.: The atmospheric boundary layer, Earth-Science Reviews, 37, 89–134, 1994.

Gerber, H., Frick, G., Malinowski, S. P., Jonsson, H., Khelif, D., and Krueger, S. K.: Entrainment rates and microphysics in POST stratocumulus, Journal of Geophysical Research: Atmospheres, 118, 12–094, 2013.

Gerber, H. E., Frick, G. M., Jensen, J. B., and Hudson, J. G.: Entrainment, mixing, and microphysics in trade-wind cumulus, Journal of the

870 Meteorological Society of Japan. Ser. II, 86, 87–106, 2008.

Griffin, K. P., Wei, N. J., Bodenschatz, E., and Bewley, G. P.: Control of long-range correlations in turbulence, Experiments in Fluids, 60, 55, 2019.

Hamlington, P. E., Poludnenko, A. Y., and Oran, E. S.: Intermittency in premixed turbulent reacting flows, Physics of Fluids, 24, 075 111, 2012.

875 Hanson, J.: Rotations in three, four, and five dimensions, arXiv preprint arXiv:1103.5263, 2011.

Horst, T. and Oncley, S.: Corrections to inertial-range power spectra measured by CSAT3 and Solent sonic anemometers, 1. Path-averaging errors, Boundary-Layer Meteorology, 119, 375–395, 2006.

Hsieh, C.-I. and Katul, G. G.: Dissipation methods, Taylor's hypothesis, and stability correction functions in the atmospheric surface layer, Journal of Geophysical Research: Atmospheres, 102, 16 391–16 405, 1997.

880 Jørgensen, F. E.: How to measure turbulence with hot-wire anemometers: a practical guide, Dantec Dynamics, 2001.

Kolmogorov, A.: The Local Structure of Turbulence in Incompressible Viscous Fluid for Very Large Reynolds' Numbers, in: Akademiia Nauk SSSR Doklady, vol. 30, pp. 301–305, 1941.

Kolmogorov, A. N.: A refinement of previous hypotheses concerning the local structure of turbulence in a viscous incompressible fluid at high Reynolds number, Journal of Fluid Mechanics, 13, 82–85, 1962.

885 Kolmogorov, A. N.: Dissipation of energy in the locally isotropic turbulence, Proceedings of the Royal Society of London. Series A: Mathematical and Physical Sciences, 434, 15–17, 1991.

Kraichnan, R. H.: Kolmogorov's hypotheses and Eulerian turbulence theory, The Physics of Fluids, 7, 1723–1734, 1964.

Küchler, C.: Measurements of Turbulence at High Reynolds Numbers, Ph.D. thesis, Georg-August-Universität Göttingen, 2021.

Küchler, C., Bewley, G., and Bodenschatz, E.: Experimental study of the bottleneck in fully developed turbulence, Journal of Statistical

890 Physics, 175, 617–639, 2019.

Küchler, C., Bodenschatz, E., and Bewley, G. P.: Scaling in Decaying Turbulence at High Reynolds Numbers, arXiv preprint arXiv:2006.10993, 2020.

Lalescu, C., Teaca, B., and Carati, D.: Implementation of high order spline interpolations for tracking test particles in discretized fields, Journal of Computational Physics, 229, 5862–5869, https://www.sciencedirect.com/science/article/pii/S002199910900607X, 2010.

895 Lalescu, C. C., Bramas, B., Rampp, M., and Wilczek, M.: An efficient particle tracking algorithm for large-scale parallel pseudo-spectral simulations of turbulence, Computer Physics Communications, p. 108406, 2022.

Lefeuvre, N., Thiesset, F., Djenidi, L., and Antonia, R.: Statistics of the turbulent kinetic energy dissipation rate and its surrogates in a square cylinder wake flow, Physics of Fluids, 26, 095 104, 2014.

Lenschow, D., Mann, J., and Kristensen, L.: How long is long enough when measuring fluxes and other turbulence statistics?, Journal of
900 Atmospheric and Oceanic Technology, 11, 661–673, 1994.

Lenschow, D. H. and Kristensen, L.: Uncorrelated noise in turbulence measurements, Journal of Atmospheric and Oceanic Technology, 2, 68–81, 1985.

Lewis, J. M., Koster, T. W., and LaRue, J. C.: On the determination of the dissipation rate of turbulence kinetic energy, Experiments in Fluids, 62, 1–13, 2021.

905 Li, X.-Y., Brandenburg, A., Svensson, G., Haugen, N. E., Mehlig, B., and Rogachevskii, I.: Condensational and collisional growth of cloud droplets in a turbulent environment, Journal of the Atmospheric Sciences, 77, 337–353, 2020.

Lumley, J.: Interpretation of time spectra measured in high-intensity shear flows, The Physics of Fluids, 8, 1056–1062, 1965.

Lumley, J.: Some comments on turbulence, Physics of Fluids A: Fluid Dynamics, 4, 203–211, 1992.

Malinowski, S. P., Gerber, H., Plante, J.-L., Kopec, M., Kumala, W., Nurowska, K., Chuang, P., Khelif, D., Haman, K., et al.: Physics of
910 Stratocumulus Top (POST): turbulent mixing across capping inversion, Atmospheric Chemistry and Physics, 13, 12 171–12 186, 2013.

McComb, W. D., Berera, A., Salewski, M., and Yoffe, S.: Taylor's (1935) dissipation surrogate reinterpreted, Physics of Fluids, 22, 061 704, 2010.

Muschinski, A. and Lenschow, D. H.: Future directions for research on meter-and submeter-scale atmospheric turbulence, Bulletin of the American Meteorological Society, 82, 2831–2843, 2001.

915 Muschinski, A., Frehich, R., Jensen, M., Hugo, R., Hoff, A., Eaton, F., and Balsley, B.: Fine-scale measurements of turbulence in the lower troposphere: An intercomparison between a kite-and balloon-borne, and a helicopter-borne measurement system, Boundary-layer meteorology, 98, 219–250, 2001.

Muschinski, A., Frehlich, R. G., and Balsley, B. B.: Small-scale and large-scale intermittency in the nocturnal boundary layer and the residual layer, Journal of Fluid Mechanics, 515, 319, 2004.

920 Nobach, H. and Tropea, C.: A statistical method for transforming temporal correlation functions from one-point measurements into longitu- dinal spatial and spatio-temporal correlation functions, Experiments in Fluids, 53, 1815–1821, 2012.

Nowak, J. L., Siebert, H., Szodry, K.-E., and Malinowski, S. P.: Coupled and decoupled stratocumulus-topped boundary layers: turbulence properties, Atmospheric Chemistry and Physics Discussions, pp. 1–41, 2021.

Obukhov, A.: Some specific features of atmospheric turbulence, Journal of Geophysical Research, 67, 3011–3014, 1962.

925 O'Connor, E. J., Illingworth, A. J., Brooks, I. M., Westbrook, C. D., Hogan, R. J., Davies, F., and Brooks, B. J.: A method for estimating the turbulent kinetic energy dissipation rate from a vertically pointing Doppler lidar, and independent evaluation from balloon-borne in situ measurements, Journal of Atmospheric and Oceanic Technology, 27, 1652–1664, 2010.

Oncley, S. P., Friehe, C. A., Larue, J. C., Businger, J. A., Itsweire, E. C., and Chang, S. S.: Surface-layer fluxes, profiles, and turbulence measurements over uniform terrain under near-neutral conditions, Journal of Atmospheric Sciences, 53, 1029–1044, 1996.

Pearson, B., Krogstad, P.-Å., and Van De Water, W.: Measurements of the turbulent energy dissipation rate, Physics of Fluids, 14, 1288–1290, 2002.

Pope, S. B.: Turbulent flows, Cambridge University Press, 2000.

Pumir, A. and Wilkinson, M.: Collisional aggregation due to turbulence, Annual Review of Condensed Matter Physics, 7, 141–170, 2016.

Risius, S., Xu, H., Di Lorenzo, F., Xi, H., Siebert, H., Shaw, R., and Bodenschatz, E.: Schneefernerhaus as a mountain research station for clouds and turbulence, Atmospheric Measurement Techniques, 2015.

Robertson, H.: The invariant theory of isotropic turbulence, in: Mathematical Proceedings of the Cambridge Philosophical Society, vol. 36, pp. 209–223, Cambridge University Press, 1940.

Shaw, R. A.: Particle-turbulence interactions in atmospheric clouds, Annual Review of Fluid Mechanics, 35, 183–227, 2003.

Siebert, H., Lehmann, K., and Wendisch, M.: Observations of small-scale turbulence and energy dissipation rates in the cloudy boundary layer, Journal of the Atmospheric Sciences, 63, 1451–1466, 2006.

Siebert, H., Gerashchenko, S., Gylfason, A., Lehmann, K., Collins, L., Shaw, R., and Warhaft, Z.: Towards understanding the role of turbulence on droplets in clouds: in situ and laboratory measurements, Atmospheric research, 97, 426–437, 2010.

Siebert, H., Beals, M., Bethke, J., Bierwirth, E., Conrath, T., Dieckmann, K., Ditas, F., Ehrlich, A., Farrell, D., Hartmann, S., et al.: The fine-scale structure of the trade wind cumuli over Barbados–an introduction to the CARRIBA project, Atmospheric Chemistry and Physics, 2013.

Siebert, H., Shaw, R., Ditas, J., Schmeissner, T., Malinowski, S., Bodenschatz, E., and Xu, H.: High-resolution measurement of cloud microphysics and turbulence at a mountaintop station, Atmospheric Measurement Techniques, 2015.

Sinhuber, M.: On the scales of turbulent motion at high Reynolds numbers, Ph.D. thesis, PhD thesis, Georg-August-Universität Göttingen, 2015.

Sinhuber, M., Bodenschatz, E., and Bewley, G. P.: Decay of turbulence at high Reynolds numbers, Physical Review Letters, 114, 034 501, 2015.

Smalikho, I., Banakh, V., Pichugina, Y., Brewer, W., Banta, R., Lundquist, J., and Kelley, N.: Lidar investigation of atmosphere effect on a wind turbine wake, Journal of Atmospheric and Oceanic Technology, 30, 2554–2570, 2013.

Sreenivasan, K.: Possible effects of small-scale intermittency in turbulent reacting flows, Flow, Turbulence and Combustion, 72, 115–131, 2004.

Sreenivasan, K., Prabhu, A., and Narasimha, R.: Zero-crossings in turbulent signals, Journal of Fluid Mechanics, 137, 251–272, 1983.

Sreenivasan, K., Deshpande, S., Prabhu, A., and Viswanath, P.: The energy dissipation in turbulent shear flows, in: Symposium on Developments in Fluid Dynamics and Aerospace Engineering, pp. 159–190, Interline Publishers, Bangalore, 1995.

Sreenivasan, K. R.: On the scaling of the turbulence energy dissipation rate, The Physics of Fluids, 27, 1048–1051, 1984.

Sreenivasan, K. R.: On the universality of the Kolmogorov constant, Physics of Fluids, 7, 2778–2784, 1995.

Sreenivasan, K. R.: An update on the energy dissipation rate in isotropic turbulence, Physics of Fluids, 10, 528–529, 1998.

Sreenivasan, K. R.: Turbulent mixing: A perspective, Proceedings of the National Academy of Sciences, 116, 18 175–18 183, 2019.

Sreenivasan, K. R. and Antonia, R.: The phenomenology of small-scale turbulence, Annual Review of Fluid Mechanics, 29, 435–472, 1997.

Taylor, G. I.: Statistical theory of turbulenc, Proceedings of the Royal Society of London. Series A-Mathematical and Physical Sciences, 151, 421–444, 1935.

Taylor, G. I.: The spectrum of turbulence, Proceedings of the Royal Society of London. Series A-Mathematical and Physical Sciences, 164, 476–490, 1938.

Tennekes, H.: Eulerian and Lagrangian time microscales in isotropic turbulence, Journal of Fluid Mechanics, 67, 561–567, 1975.

Tritton, D.: Physical Fluid Dynamics, 1977.

970 Vallikivi, M., Hultmark, M., Bailey, S. C. C., and Smits, A.: Turbulence measurements in pipe flow using a nano-scale thermal anemometry probe, Experiments in Fluids, 51, 1521–1527, 2011.

Vassilicos, J. C.: Dissipation in turbulent flows, Annual Review of Fluid Mechanics, 47, 95–114, 2015.

Wacławczyk, M., Ma, Y.-F., Kopeć, J. M., and Malinowski, S. P.: Novel approaches to estimating the turbulent kinetic energy dissipation rate from low-and moderate-resolution velocity fluctuation time series, Atmospheric Measurement Techniques, 10, 4573–4585, 2017.

975 Wacławczyk, M., Gozingan, A. S., Nzotungishaka, J., Mohammadi, M., and P Malinowski, S.: Comparison of Different Techniques to Calculate Properties of Atmospheric Turbulence from Low-Resolution Data, Atmosphere, 11, 199, 2020.

Warhaft, Z.: Passive scalars in turbulent flows, Annual Review of Fluid Mechanics, 32, 203–240, 2000.

Wilczek, M. and Narita, Y.: Wave-number–frequency spectrum for turbulence from a random sweeping hypothesis with mean flow, Physical Review E, 86, 066 308, 2012.

980 Wilczek, M., Xu, H., and Narita, Y.: A note on Taylor's hypothesis under large-scale flow variation, Nonlin. Processes Geophys, 21, 645–649, 2014.

Willis, G. and Deardorff, J.: On the use of Taylor's translation hypothesis for diffusion in the mixed layer, Quarterly Journal of the Royal Meteorological Society, 102, 817–822, 1976.

Wyngaard, J. and Clifford, S.: Taylor's hypothesis and high–frequency turbulence spectra, Journal of the Atmospheric Sciences, 34, 922–929, 985 1977.

Wyngaard, J. C.: Atmospheric turbulence, Annual Review of Fluid Mechanics, 24, 205–234, 1992.

Wyngaard, J. C.: Turbulence in the Atmosphere, Cambridge University Press, 2010.